RSC Advances

PAPER

View Article Online
View Journal | View Issue

Cite this: *RSC Adv.*, 2026, **16**, 2428

P,N-doped nickel–carbon nanofibers derived from ammonium phosphate for efficient glycerol electrooxidation and renewable power generation from biodiesel waste

Nasser A. M. Barakat, *[ab] Ahmed Saadawi[a] and Shimaa Hamda[a]

Received 30th October 2025
Accepted 3rd January 2026

DOI: 10.1039/d5ra08367b

rsc.li/rsc-advances

Nickel electrocatalysts present an economic alternative to noble metals for alcohol oxidation in alkaline fuel cells. Here, P,N-doped Ni-containing carbon nanofibers (Ni-CNFs) were synthesized by electrospinning of nickel acetate solutions with ammonium phosphate followed by thermal stabilization and calcination. Phosphate and nitrogen dopants regulated the electronic structure and surface chemistry of the nanofibers, which promoted the formation of active NiOOH species for catalysis. X-ray diffraction (XRD) and transmission electron microscopy (TEM) confirmed the formation of a metallic nickel (Ni^0)/graphitic carbon nanofiber (CNF) hybrid with nanoscale dispersion of nickel domains, while X-ray photoelectron spectroscopy (XPS) verified the coexistence of Ni^0/Ni^{2+} species together with phosphate (P^{5+}–O) and nitrogen–carbon (N–C) functionalities, which collectively promote redox reversibility. Electrochemical activation in 1.0 M KOH yielded a high electrochemical surface area (~40 600 $cm^2\ g^{-1}$) and distinct Ni(II)/Ni(III) redox transitions. The optimized 1 wt% DAP-Ni-CNF electrode achieved a glycerol oxidation current density of ~140 mA cm^{-2} in 0.25 M glycerol with an apparent activation energy of ~15 kJ mol^{-1}, which points towards fast charge transfer through a NiOOH-mediated pathway. In direct glycerol fuel cell tests, the same electrode achieved a peak power density of ~200 mW m^{-2} at 1.0 M glycerol. Notably, this study demonstrates that glycerol that is collected as a waste by-product from biodiesel production can be utilized as a viable new renewable energy source, valorizing low-value residues to clean electricity. The developed P,N-doped Ni-CNFs thus provide a sustainable route for glycerol valorization and circular bioenergy generation through alkaline fuel cell technology.

1 Introduction

The increasing global energy requirement and the need to reduce carbon emissions have spurred efforts to make sustainable and renewable energy technologies. Of the several clean-energy strategies, the use of chemical energy stored in compounds made from biomass to generate electricity by electrochemical processes has attracted universal interest.[1] These technologies, besides providing renewable energy, support the concepts of circular economy in that they utilize industrial waste and low-value residues as feedstock.[2]

Biodiesel manufacture is one of the prominent avenues for sustainable transportation fuel, producing approximately 10 wt% of glycerol as a by-product.[3] With the ever-increasing industries producing biodiesel worldwide, massive quantities of glycerol are produced annually, leading to severe overproduction and sharp decline in its market price. Crude glycerol purification is typically not economically feasible due to the presence of methanol, soaps, and salts.[4] Thus, glycerol tends to be considered an industrial by-product, and it poses environmental as well as economic disposal problems. Therefore, valorizing such a common by-product in catalytic or electrochemical directions has been a key step in the improvement of the overall sustainability of the biodiesel value chain.[5,6]

The direct glycerol fuel cell represents a promising route towards the conversion of glycerol to electrical energy.[7] This response couples anodic glycerol oxidation with cathodic oxygen reduction in basic conditions. Glycerol oxidation is particularly desirable because of its high theoretical energy density ($6e^-$ per molecule) as well as the simultaneous creation of value-added intermediates such as glycerate, glycolate, and formate.[8] Unlike methanol or ethanol oxidation, the reaction of glycerol oxidation (GOR) involves less onset potential, higher electron yield, and less CO_2 emission and therefore is a more environmentally acceptable choice for small-scale renewable fuel cells.[9]

Despite these advantages, the practical realization of direct glycerol fuel cells (DGFCs) remains impeded by the non-

[a]*Chemical Engineering Department, Faculty of Engineering, Minia University, El-Minia 61516, Egypt. E-mail: nasbarakat@mu.edu.eg; Tel: +20862321407*
[b]*Chemical Engineering Department, Faculty of Engineering, Atatürk University, 25240, Erzurum, Turkey*

availability of efficient, cost-effective, and long-lasting anode catalysts. The noble metals Pt, Pd, and Au are extremely active at the start but are prone to high cost, low abundance, and poisoning by the strongly adsorbed intermediates with eventual deactivation in extended use.[10] Consequently, there has been a growing need for earth-abundant transition-metal catalysts. Catalysts based on nickel have emerged as particularly promising candidates as alkaline medium polyalcohol oxidation catalysts. Nickel shows high intrinsic activity owing to the reversible Ni(II)/Ni(III) redox couple, where reduction of $Ni(OH)_2$ to NiOOH forms the true active sites for alcohol oxidation. However, pure Ni catalysts are normally suffered by poor long-term stability, low conductivity, and limited reversibility of redox.[11–13]

In order to overcome these disadvantages, heteroatom doping has been recognized as an effective approach to modulate electronic and surface properties of Ni-based materials. Particularly, phosphorus and nitrogen dopants can form harmless charge distributions, enhance hydrophilicity, and increase hydroxide ion adsorption towards the development of the active NiOOH phase.[14,15] Surface stabilizing phosphate species can also help to prevent over-oxidation of Ni and improve tolerance towards reaction intermediates.[16] In contrast, nitrogen incorporation enhances electronic conductivity, creates defect-rich carbon structures, and more effectively anchors metal nanoparticles, inhibiting their agglomeration upon electrochemical cycling.[17,18] Synergistic action of such dopants should significantly increase the catalytic activity and long-term durability of Ni-based electrodes.

To this end, CNFs have drawn extensive attention as exemplary supports for electrocatalysts due to their superior electrical conductivity, high surface area, and better mechanical stability. Electrospinning is an adjustable and scalable technique to produce homogeneous CNFs with designed morphology and regulated composition. The technique also provides a pathway to feed directly metal salts and dopant precursors into the polymeric spinning solution, making it possible to form metal–carbon composites with evenly dispersed nanoparticles during carbonization.[19,20]

Taking these advantages, the present work applies ammonium phosphate as a bimodal dopant precursor that collectively introduces phosphorus and nitrogen into Ni-CNFs both through electrospinning and post-heating. Two forms of ammonium phosphate—mono-ammonium phosphate (MAP) and di-ammonium phosphate (DAP)—were employed to explore the composition effect on structure and electrochemical activity of the resulting products. This strategy is facilitated by the capability of controlling the P/N ratio with high precision as well as the application of a low-cost, sustainable source of dopant. The P,N-doped Ni-dispersed CNFs prepared using this method are expected to possess enhanced Ni dispersion, electron transfer, and density of catalytically active sites by virtue of metal–support interactions and phosphate stabilization.

Although various investigations of Ni-based catalysts for methanol and ethanol oxidation are common, methodical publications on ammonium phosphate-sourced P,N co-doped Ni-CNFs for the oxidation of glycerol as well as their application in direct glycerol fuel cells are scarce. It is also crucial to know the dopant chemistry–surface redox behavior–performance correlation to prepare emerging non-noble metal-based catalysts.

Thus, in this paper, the synthesis, characterization, and electrochemical activity of P,N-doped Ni-CNFs prepared from mono- and di-ammonium phosphate precursors are presented. High-powered characterization by XRD, TEM, and XPS confirm that the presence of phosphate and nitrogen dopants significantly changes the nanofiber crystallinity and surface chemistry, improving the formation of catalytically active Ni^0/NiOOH interfaces. Most notably, though, this study demonstrates that glycerol—a waste stream and by-product of the process of producing biodiesel—can be directly utilized as a renewable energy source in a highly efficient conversion of industrial waste into clean energy. The findings set the proposed P,N-doped Ni-CNFs as an effective and viable platform for waste-to-electricity conversion in accordance with efforts towards integrating circular bioenergy systems into the renewable energy framework.

2 Materials and methods

2.1 Materials

Nickel(II) acetate tetrahydrate ($Ni(CH_3COO)_2 \cdot 4H_2O$, ≥98%), mono-ammonium phosphate ($NH_4H_2PO_4$, ≥99%), and di-ammonium hydrogen phosphate ($(NH_4)_2HPO_4$, ≥99%) were purchased from Sigma-Aldrich and used as the nickel source and dual phosphorus/nitrogen dopant precursors, respectively. Poly(vinyl alcohol) (PVA, $M_w \approx$ 85 000–124 000, 99+% hydrolyzed, Merck) was used as the carbon precursor and fiber-forming polymer for electrospinning. Ethanol (≥99.8%) and deionized water (18.2 MΩ cm) were used as solvents during solution preparation and post-processing. Poly(vinylidene fluoride) (PVDF, Sigma-Aldrich) was used as the binder for the fabrication of working electrodes and was dissolved in *N*,*N*-dimethylformamide (DMF, ≥99.8%, Fisher Scientific) to form the slurry. To prepare the catalyst ink for three-electrode electrochemical testing, the Nafion® solution (5 wt%) from Sigma-Aldrich and isopropanol (≥99.5%, Fisher Scientific) were used as dispersing and ion-conducting agents.

Electrochemical measurements were performed in 1.0 M KOH aqueous electrolyte prepared from analytical-grade potassium hydroxide pellets (≥85%, Merck). Glycerol ($C_3H_8O_3$, ≥99.5%, Fisher Scientific) was used as model fuel at concentrations between 0.05–1.0 M for cyclic voltammetry and 0.05–2.0 M for DGFC testing. The electrochemical system utilized a standard three-electrode configuration containing a glassy carbon (GC) working electrode, a platinum wire counter electrode, and an Ag/AgCl (3 M KCl) reference electrode; all potentials are reported *versus* Ag/AgCl unless otherwise noted.

For DGFC assembly, a Pt-loaded carbon cloth cathode (20 wt% Pt on Vulcan XC-72, FuelCellStore) was used to catalyze the oxygen reduction reaction (ORR). The as-prepared Ni-CNF catalysts served as the anode material, coated on carbon cloth. The anolyte consisted of 0.25 M glycerol + 1.0 M KOH. All reagents used were of analytical grade and employed without

further purification. Electrospinning syringes, collectors, and cell components were cleaned with ethanol and dried before each test to avoid cross-contamination between different samples and test conditions.

2.2 Catalyst preparation

P,N-doped Ni-CNFs were prepared through an electrospinning–carbonization route, using nickel acetate as the metal precursor and ammonium phosphate as a dual phosphorus–nitrogen dopant source. In a typical preparation, 15 g of a 10 wt% PVA aqueous solution was made by dissolving PVA granules in deionized water under magnetic stirring at 50 °C for 5 h until a clear homogeneous solution was obtained. In a separate container, 1.0 g of nickel acetate tetrahydrate ($Ni(CH_3COO)_2 \cdot 4H_2O$) was dissolved in 5 mL of deionized water under continuous stirring. Upon complete dissolution, an appropriate amount of ammonium phosphate (0–10 wt% relative to PVA) was added into the solution of nickel acetate, either mono-ammonium phosphate (MAP) or di-ammonium hydrogen phosphate (DAP), followed by stirring for another 1 h.

The resulting metal–dopant mixture was slowly poured into the PVA solution and further stirred for 5 h at 50 °C to obtain a viscous and homogeneous electrospinning dope. The precursor solution was loaded into a 10 mL plastic syringe fitted with a stainless-steel needle (inner diameter = 0.6 mm) and electrospun under the following optimized conditions: an applied voltage of 20 kV, a tip-to-collector distance of 15 cm, and a flow rate of 0.7 mL h^{-1}. The nanofibers were collected on aluminum foil attached to a grounded rotating drum and then vacuum-dried at 60 °C overnight to remove residual moisture and solvents.

The as-spun nanofiber mats were stabilized by heating them in air at 250 °C for 3 h at a heating rate of 1 °C min^{-1}, which induced cross-linking and partial oxidation of PVA to structurally preserve the nanofibers during subsequent carbonization. Carbonization was conducted in a tube furnace under an inert atmosphere at 850 °C for 2 h with a heating rate of 5 °C min^{-1}. In this process, PVA was converted into conductive carbon nanofibers, while nickel acetate was reduced to metallic Ni nanoparticles and ammonium phosphate decomposed into gaseous species that generated P- and N-containing functionalities on the carbon matrix. The prepared samples were denoted as *x*MAP-Ni-CNFs or *x*DAP-Ni-CNFs, where *x* represents the weight percentage of ammonium phosphate (0, 1, 3, 5, 7, or 10 wt%). After being cooled to room temperature, the carbonized mats were gently ground to a fine powder for characterization and electrochemical testing.

2.3 Electrode fabrication and electrochemical measurements

The obtained P,N-doped Ni-CNF powders were prepared into working electrodes by a binder-assisted casting method for electrochemical evaluation. Typically, 2 mg catalyst powder was dispersed in a mixture containing 400 μL of isopropanol and 20 μL Nafion® solution (5 wt%). The ink obtained was ultrasonicated for 30 min to achieve a uniform suspension. A known volume, 15 μL, of the well-dispersed ink was drop-cast onto a glassy carbon GC electrode with a geometric area of 0.07014 cm^2 and dried under ambient atmosphere to form a thin uniform catalytic layer. Before coating, the GC electrode was polished with 0.05 μm alumina slurry, rinsed with deionized.

All electrochemical measurements were performed on a CHI 760E electrochemical workstation from CH Instruments, USA, with the as-prepared catalyst-coated GC serving as the working electrode in a three-electrode configuration. A platinum wire served as the counter electrode, while an Ag/AgCl electrode (3 M KCl) was used as the reference electrode. The electrolyte was 1.0 M KOH aqueous solution with and without 0.25 M glycerol. For the present work, all potentials are given with respect to Ag/AgCl unless otherwise stated.

Cyclic voltammetry (CV) was performed in the potential range of −0.2–1.0 V *vs.* Ag/AgCl at scan rates between 5 and 100 mV s^{-1} to study the redox behavior and kinetic response. The electrochemical activation of the Ni-based catalysts was monitored through the reversible Ni(II)/Ni(III) redox peaks corresponding to the formation of NiOOH active species. The electrochemically active surface area (ECSA) was estimated using the charge associated with the $Ni(OH)_2$/NiOOH transition according to the relation:

$$\mathrm{ESCA} = \frac{Q}{0.257 \times m} \quad (1)$$

where Q is the integrated charge (C) under the redox peak, m is the catalyst mass (g), and 0.257 C cm^{-2} is the standard charge required for a monolayer of NiOOH formation. CA measurements were performed at fixed potentials (usually around 0.5–0.7 V *versus* Ag/AgCl) for 1000 s to evaluate the stability and tolerance of these catalysts against the accumulation of intermediates. The same electrode was tested sequentially at different potentials in the same three-electrode cell, with each step lasting 1000 s.

Temperature-dependent CVs between 30 and 60 °C were conducted to estimate the apparent activation energy (E_a) associated with the glycerol oxidation process. The temperature of the electrolyte was controlled through a thermostatic water bath. Logarithmic relations of current density *vs.* inverse temperature (Arrhenius plots) were utilized to calculate the E_a values.

2.4 Direct glycerol fuel cell

In this work, the membrane-less direct glycerol fuel cells were set up in a parallel-plate configuration with a piece of 3.0 × 3.0 cm carbon-cloth anode facing a commercial Pt/C air cathode (20 wt% Pt on Vulcan XC-72, Pt loading 0.4 mg cm^{-2}, FuelCellStore) at a fixed inter-electrode gap of 0.5 cm. The anode catalyst layer was prepared as an ink containing 0.06 g of functional nanofibers (typically, the 1 wt% DAP-Ni-CNFs sample unless otherwise stated), 0.12 g of PVDF binder, and 1.0 mL of *N*,*N*-dimethylformamide. The slurry was magnetically stirred for ≥1 h to ensure full homogenization and then uniformly coated onto carbon cloth (3 × 3 cm) using a doctor-blade technique. After drying the electrodes in air at 80 °C to

remove residual solvent, they were thermally treated at 350 °C for 1 h to enhance adhesion and partial binder pyrolysis. Total catalyst loading was determined gravimetrically, and single-side coatings were employed throughout all DGFC experiments. Two high corrosion stainless steel sheets were used as current collector at the anode and cathode.

A CHI 760E potentiostat/galvanostat from CH Instruments (USA) was employed in a two-electrode configuration-a setup in which the Ni-CNF anode acted as the working electrode, while the Pt/C electrode was used both as a counter and as a reference electrode. The cell performance was measured after stabilizing the OCP for 5–10 min. The polarization curves were measured using LSV from the OCP to 0 V at a scan rate of 0.001 V s^{-1}. The power density (P) was determined in accordance with the relation $P = I \times V$ where I is the measured current (A), V is the corresponding cell voltage (V), and $A_{cathode}$ the apparent cathode area (0.00052 m^2) used for normalization; current densities were likewise normalized to $A_{cathode}$. Series resistance was minimized by short electrical leads and a compact cell geometry, and no post-measurement iR compensation was applied unless specified. In the case of temperature-dependent studies, the same procedure was repeated at each temperature set point after attaining thermal equilibrium. Each experiment was repeated at least twice with fresh electrolyte for reproducibility, and the polarization and power density curves obtained represent the averaged data.

2.5 Characterization

X-ray diffraction (XRD) patterns were recorded with the help of a JEOL diffractometer with Cu Kα radiation ($\lambda = 1.5406$ Å) at an operating voltage and current of 40 kV and 40 mA, respectively. The diffraction data were recorded over the 2θ range from 10 to 80° using a step width of 0.02° and a scan speed of 1° min^{-1}. Identification of the crystalline phases was performed by comparing the experimental patterns with standard data from the ICDD-PDF-4+ database. SEM analyses were performed on a JEOL JSM-7610F field-emission microscope to assess the surface morphology, fiber diameter distribution, and structural uniformity of the electrospun nanofibers before and after carbonization. The samples were fixed on conductive carbon tape and sputter-coated with a thin layer of gold to prevent charging during imaging.

Internal nanostructure, dispersion of the Ni nanoparticles, and their crystallinity were analyzed using transmission electron microscopy (TEM) on a JEOL JEM-2100 instrument operating at 200 kV. The interplanar spacings were determined based on high-resolution TEM images, where lattice fringes corresponding to specific Ni and graphitic carbon planes were identified. SAED patterns were obtained from representative regions to confirm the polycrystalline metallic Ni phase in these samples and further determine the degree of graphitization of the CNF matrix.

XPS measurements were performed in a Thermo Scientific K-Alpha+ spectrometer equipped with a monochromatic Al Kα source (1486.6 eV). The binding energies were calibrated using the C 1s peak at 284.6 eV as a reference. High-resolution spectra of Ni 2p, C 1s, O 1s, N 1s, and P 2p were recorded to investigate the oxidation states of nickel and the chemical bonding environments of the incorporated elements. Deconvolution was carried out for all spectra using CasaXPS software with a Shirley background and Gaussian–Lorentzian peak fitting. Elemental compositions were determined from the corresponding peak areas corrected by sensitivity factors.

3 Results and discussion

Prior to heat treatment, nickel acetate is dissolved with mono- or di-ammonium phosphate to add Ni^{2+} with phosphate species ($H_2PO_4^-$/HPO_4^{2-}/PO_4^{3-}). There are chances for partial ion pairing or precipitation of hydrated nickel phosphate under such conditions:

$$3Ni^{2+} + 2PO_4^{3-} + xH_2O \rightarrow Ni_3(PO_4)_2 \cdot xH_2O(s) \quad (2)$$

The XRD pattern of the ammonium-phosphate-derived Ni carbon nanofibers (7 wt% DAP, Fig. 1) shows the three characteristic fcc metallic Ni reflections at $2\theta = 44.8°$, 52.2°, and 76.8°, referring to the (111), (200), and (220) planes, respectively (reference fcc-Ni; *e.g.*, JCPDS 04-0850). These are shifted to slightly higher 2θ than nominal positions (44.507°, 51.89°, and 76.37°), indicating a minor lattice contraction. Such upshifts are generally accounted for by one or more of: (i) microstrain with the nanoscale crystallites and quick carbothermal reduction; (ii) solid-solution-type light-element inclusion (*e.g.*, any remaining P/C from the phosphate/carbon environment) that could compress the Ni lattice; and/or (iii) slight variations in instrumental calibration. JADE matching set down metallic Ni as the major crystalline phase; no sign was observed for NiO. Besides the three pronounced Ni peaks, several weaker ones are at ~36.8°, 42.2°, 44.0°, 47.0°, and 55.8° (very small):

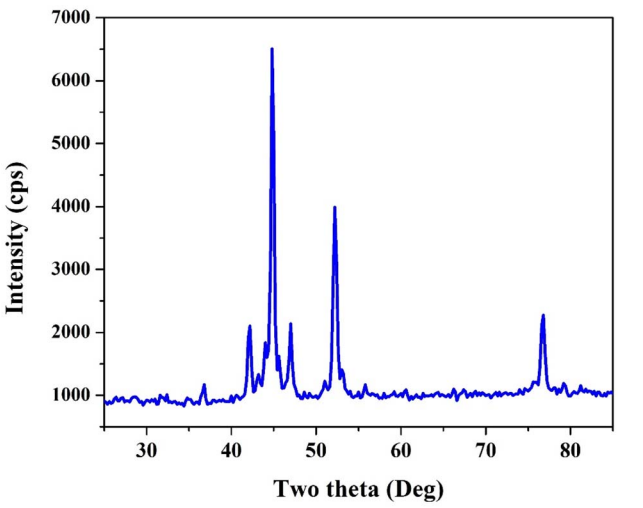

Fig. 1 X-ray diffraction pattern of ammonium-phosphate-derived Ni-CNFs (7 wt% DAP) showing fcc-Ni reflections at 44.8°, 52.2°, and 76.8° indexed to (111), (200), and (220), respectively (JCPDS 04-0850). Small additional features in the 36–56° range overlap with graphitic carbon and possible P-containing Ni species.

• The 42.2° band is likely to overlap with the (100) turbostratic/graphitic carbon reflection, while the shoulder at ~44.0° may be due to contributions from graphitic (101) and the prominent Ni(111) envelope.[21]

• The low-intensity weak peaks at ~47.0° and ~55.8° occur in a region where nickel phosphide substoichiometries (*e.g.*, Ni_2P/Ni_3P series of families derived from phosphate precursors) and higher-order graphitic layers (*e.g.*, (004) ≈54–55° for partially graphitized carbons) both generally diffract.[22,23]

• The low-intensity peak at ~36.8° could be due to defect-rich carbon or phosphide-related reflections, but not sufficient for sole indexing.

Zero-valent metallic nickel formation rather than the expected oxide form can be attributed by the following reason. When heated in inert atmosphere, ammonium phosphate deammoniates/dehydrates to poly-/metaphosphate species and acetate/PVA pyrolysis produces CO and H_2. Nickel-phosphate or NiO intermediates are then reducible to metallic Ni due to the abnormal of the unreacted nickel acetate under inert atmosphere.[24,25]

$$Ni(CH_3COO)_2\cdot 4H_2O \rightarrow 0.86Ni(CH_3COO)_2\cdot 0.14Ni(OH)_2 + 0.28CH_3COOH + 3.72H_2O \quad (3)$$

$$3(0.86\ Ni(CH_3COO)_2\cdot 0.14Ni(OH)_2) + 0.28H_2O \rightarrow 3NiCO_3 + 2.44CH_3COCH_3 + 1.12H_2 \quad (4)$$

$$NiCO_3 \rightarrow NiO + CO_2 \quad (5)$$

$$NiO + CO/H_2 \rightarrow Ni + CO_2/H_2O \quad (6)$$

Overall, XRD verifies that the scaffold nanofiber contains crystalline fcc-Ni nanoparticles in a partially graphitized carbon matrix with minor lattice contraction relative to bulk Ni. Such architecture is favorable for glycerin electrooxidation: metal Ni offers high electronic conductivity and offers Ni^0/Ni^{2+} redox sites upon alkaline polarization, whereas the conductive carbon matrix offers charge transport and distributes the active metal sites. Any phosphorus-derived species (phosphide or surface phosphate) that might be present at low levels—though not resolvable here—are known to modulate Ni's electronic structure and adsorption energetics, potentially aiding alcohol (polyol) activation; this point is treated more fully in the surface-chemistry/XPS section.

Inclusion of ammonium phosphate and chemical composition of utilized dopant (*i.e.* mono or di or tri-ammonium phosphate) has particular effect on morphology of nanofibers as is clear from the SEM micrographs (Fig. 2). As can be seen in Fig. 2A, calcination of nanofiber mats without ammonium phosphate resulted in coherent non-woven of continuous, cylindrical filaments. Surfaces are especially smooth and free from beading, evidencing a consistent whipping regime and good chain entanglement during spinning. Homogeneous topology indicates elimination of solvent without capillary breakup and preservation of an inter-percolated network of fibers that is useful for electron conduction upon thermal treatment.

On the other hand, as indicated by Fig. 2B, the introduction of a small amount of mono-ammonium phosphate (1 wt%) transforms the skin of the fiber from smooth to finely nodular. The filaments are unbroken, though there is a dense, sub-100 nm "pebbled" surface that covers the circumference homogeneously. Such stippling is anticipated in in-jet complexation/incipient precipitation in between Ni^{2+} and phosphate species as evaporation of the jet occurs, presenting numerous nucleation sites imbedded within the polymer matrix. Upon calcination these nuclei are converted to Ni-containing nanoparticles anchored at the surface, effectively presenting accessible surface area with the mechanical stability of the mat remaining unaffected.

With di-ammonium phosphate (Fig. 2C) at the same nominal load, salt effect is more marked. Fibers are heavily coated by nanoparticles and small clusters, and singly isolated faceted particulates are evident in amongst filaments. The greater dope basicity/ionic strength likely enhances solution conductivity and screens polymer–polymer interactions, favoring early nucleation and localized jet destabilization. So, some of the inorganic phase appears as discrete particles rather than being confined to a thin shell on the fiber, creating a rough, heterogeneous surface and fuzzy fiber contours locally.

For tri-ammonium phosphate, in the same conditions, ammoniated phosphate feed was unable to be electrospun. The probable cause is an unfavorable ratio of viscosity, surface

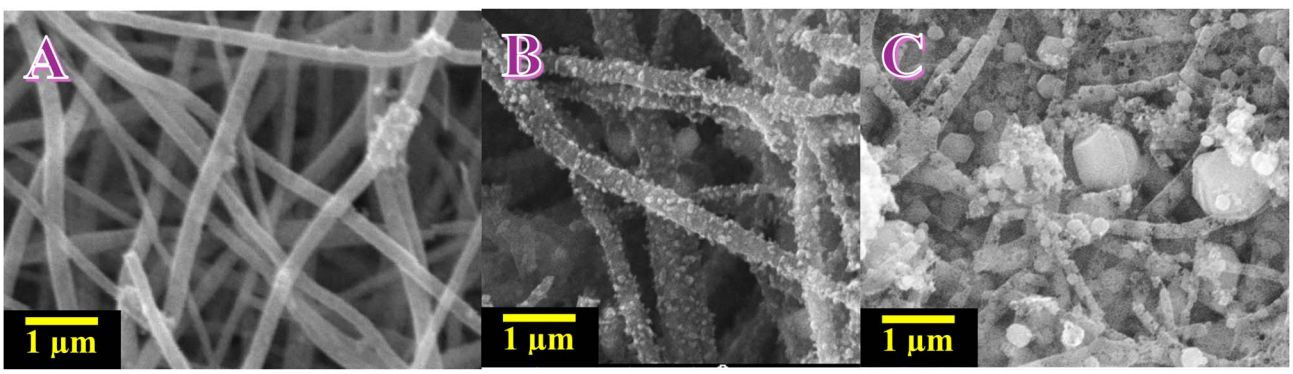

Fig. 2 SEM images for the nanofibers obtained from calcination of different electrospun mats: (A) ammonium phosphate-free, (B) mono ammonium phosphate-containing and (C) di ammonium phosphate-containing.

tension, and conductivity: strong ion-polymer/ion-Ni^{2+} interactions reduce effective chain entanglement while the high ionic strength favors electrospraying at the cost of continuous filament formation.

Together, phosphate is a morphology modulator. The mono-ammonium phosphate case study (Fig. 2B) produces highly decorated, high-area fibers that retain network cohesion—a good structure for catalytic/electrochemical use. The di-ammonium phosphate case study (Fig. 2C) maximizes roughness but incorporates coarser aggregates, which may reduce uniformity and partially clog pore channels. The observed hierarchy—smooth (no phosphate) through nodular (mono) to over-ornamented with secondary particulates (di)—is fully consistent with phosphate-assisted nucleation of Ni-containing species upon drying and fixation onto/around the surface of the nanofiber upon subsequent heat treatment.

Fig. 3A is TEM micrograph of Ni carbon nanofibers derived from mono-ammonium phosphate. The structure evidently confirms the fibrous nature having dark nanoparticles dispersed in it, indicating the effective impregnation of the Ni species within the carbon nanofiber backbone. The nanofibers are continual in nature with average diameter 150–200 nm and the Ni nanoparticles are dispersed over the surface of the fibers and in the matrix. Particle sizes of dispersed particles vary between ~47 and 57 nm, with a few large agglomerates indicating ~160 nm. The hierarchical distribution reflects that phosphate-assisted synthesis provides a good condition for growth and nucleation, leading to comparatively homogeneous dispersion of Ni particles over the conductive carbon framework. The proximity of metal nanoparticles to the carbon substrate is expected to improve electrical conductivity as well as electron transfer during oxidation of glycerin.

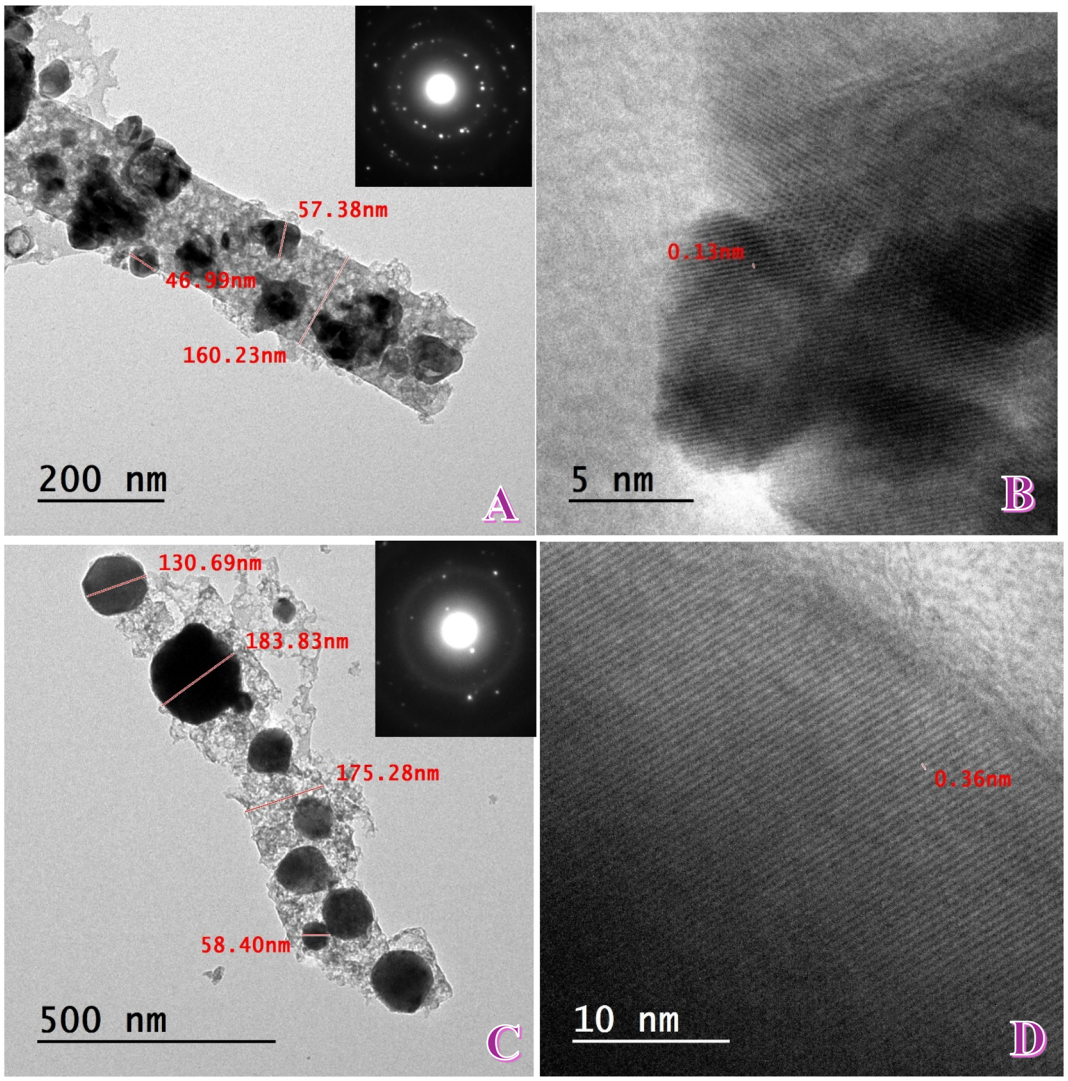

Fig. 3 TEM and HRTEM images of ammonium phosphate-derived Ni-CNFs. (A) TEM of mono-ammonium phosphate-based nanofibers showing well-dispersed Ni nanoparticles with an average size of ~50–160 nm; inset: SAED pattern confirming fcc-Ni crystallinity. (B) HRTEM of MAP-based nanofibers showing Ni(111) lattice fringes with *d*-spacing of ~0.213 nm. (C) TEM of di-ammonium phosphate (DAP)-based nanofibers displaying larger Ni nanoparticles ranging from ~58–184 nm; inset: SAED pattern showing polycrystalline Ni rings. (D) HRTEM of DAP-based nanofibers showing graphitic (002) fringes with *d*-spacing of ~0.36 nm.

The SAED pattern (inset of Fig. 3A) exhibits concentric diffraction rings and individual bright spots, confirming the polycrystalline character of the Ni nanoparticles. The rings are (111), (200), and (220) planes of fcc (face-centered cubic) Ni, as from the XRD data. The lack of other rings that are well defined in NiO is consistent with the XRD result that the dominant crystalline phase is Ni, and there is minimal indication of bulk NiO formation. Sharpness of the diffraction spots within the rings also points to crystalline nanoparticles with ordered domains, which is good for catalytic activity.

High-resolution TEM (HRTEM) imaging (Fig. 3B) provides additional information on the nanoparticle crystallinity locally. The lattice fringes are resolved clearly with an interplanar spacing of ~0.213 nm, which is almost identical to the *d*-spacing of the Ni (111) plane. This is consistent with the fact that the nanoparticles are predominantly metallic Ni and supports the limited shifting of diffraction peaks presented in the XRD analysis. The regular lattice fringes demonstrate the good crystallinity of Ni domains, which is desirable because crystalline Ni sites can potentially act as good electroactive centers in polyol oxidation reactions.[26] The dense interface between Ni nanoparticles and carbon also suggests strong metal–support interaction, which keeps the nanoparticles from sintering and enhances their catalytic stability.[27]

Together, the TEM, SAED, and HRTEM characterizations confirm that the mono-ammonium phosphate-derived Ni-CNFs consist of crystalline fcc-Ni nanoparticles evenly dispersed over a conductive carbon nanofiber support. The phosphate precursor is engaged in controlling Ni particle nucleation and distribution, and the carbon nanofiber scaffold provides structural integrity and charge-conductive channels. Synergy in the resultant architecture is expected to facilitate efficient electron/ion transport, enhanced stability, and improved catalytic activity for glycerin electrooxidation.

Fig. 3C presents the TEM image of the di-ammonium phosphate-derived Ni carbon nanofibers. Compared to the MAP-based fibers (Fig. 3A), the DAP-based fibers exhibit a relatively larger Ni nanoparticle size distribution, ranging from ~58 to 184 nm. A few particles are over 130 nm, indicating that the use of di-ammonium phosphate results in more severe particle growth and aggregation during the calcination process. Even with this increased particle size, the nanoparticles are still bound within the carbon matrix, providing stability. The wider distribution indicates that the decomposition pathway of DAP gives greater reducing gases and P-based intermediates, which enhance Ni nucleation but could also enhance particle coalescence. In contrast, the sample based on MAP exhibited a narrower size range, showing more particle dispersion.

The SAED pattern (inset of Fig. 3C) shows bright spots on sharp polycrystalline diffraction rings, which is typical for the fcc-Ni phase. The reflections are of (111), (200), and (220) planes, established by XRD. Compared to MAP-based nanofibers, in this case, the rings are more diffuse, typical for larger particle sizes from TEM—larger crystallites produce sharper diffraction spots but reduce the number of nanocrystalline domains. This differentiation points out that the synthesis route (MAP *vs.* DAP precursor) influences both the particle size and crystalline distribution.

The HRTEM micrograph (Fig. 3D) exhibits clear lattice fringes with an interplanar spacing of 0.36 nm, matching well with the (002) plane of graphitic carbon. This reveals the formation of a partially graphitized carbon matrix to encapsulate and stabilize the Ni nanoparticles.[28] As compared with the MAP sample, where lattice fringes of Ni (111) were dominant, the nanofibers based on DAP emphasize the graphitic matrix more intensely, indicating that graphitization is preferred during decomposition of di-ammonium phosphate. High graphitic ordering is advantageous in that it provides very conductive channels for electron transport and also contributes toward stability of the overall composite framework.

Fig. 4A displays the XPS analyses for the MAP-based nanofibers. In Fig. 4A, all spectra were charge-referenced to C 1s = 284.8 eV. In every region, the convoluted fit reproduces the raw line shape after background subtraction, supporting chemically meaningful deconvolutions. Three components describe the carbon envelope. The main peak at 284.83 eV (FWHM 1.22 eV, area 5102.1 CPS eV) accounts for 64.02% of the C-signal and corresponds to sp^2/sp^3 C–C/C–H from the PVA-derived turbostratic carbon matrix.[29] Oxygenated carbon is represented by two higher-BE components: 285.79 eV (FWHM 1.84 eV, 27.49%, area 2189.9 CPS eV) assigned to C–O/C–O–C (±C–N), and 287.60 eV (FWHM 3.40 eV, 8.49%, area 675.4 CPS eV) attributed to C=O/O–C=O species. Thus, ~36% of the surface carbon is oxygen-functionalized, which explains the good wettability of the fibrous scaffold and provides potential anchoring sites for metal nanoparticles. No detectable shoulder near ~283 eV is observed, indicating the absence of a resolvable metal carbide contribution.[30]

The N 1s region (Fig. 4B) is fitted with a single component centered at 402.94 eV (FWHM 1.71 eV, area 161.4 CPS eV, 100% of the N envelope), characteristic of oxidized/positively charged nitrogen (N–O or N^+–O^-). The lack of features at 397–400 eV excludes detectable metal nitride or pyridinic/pyrrolic/graphitic N.[31] This is consistent with the ammonium precursor being volatilized during calcination (NH_3/H_2O), leaving only minute, oxidized N formed upon air exposure.[32]

Oxygen appears in three chemical states; Fig. 4C. The low-BE component at 529.33 eV (FWHM 1.34 eV, area 1203.9 CPS eV) contributes 21.93% of the O-signal and corresponds to lattice O^{2-} in Ni–O–Ni (NiO/NiO_x), evidencing the expected native oxide on Ni nanoparticles.[33] A second component at 531.12 eV (FWHM 1.82 eV, area 1438.9 CPS eV, 26.22%) is assigned to hydroxyl/defect oxygen (Ni–OH/NiOOH-like species) and non-bridging phosphate oxygen (P=O/P–O^-).[34] The higher-BE envelope at 532.42 eV (FWHM 2.72 eV, area 2839.5 CPS eV) constitutes 51.84% of the O-signal and is attributed to oxygen bound to carbon (C–O/C–O–C/O–C=O) together with adsorbed H_2O and bridging P–O–M/P–O–C environments. Altogether, roughly 48% of the O 1s intensity (529.3 + 531.1 eV) belongs to the $NiO_x(OH)_y$ surface shell, while ~52% arises from the carbon/adsorbate/phosphate oxygen.

Phosphorus (Fig. 4D) is present exclusively as phosphate (P^{5+}). The doublet is resolved at P $2p_{3/2}$ = 133.11 eV (FWHM

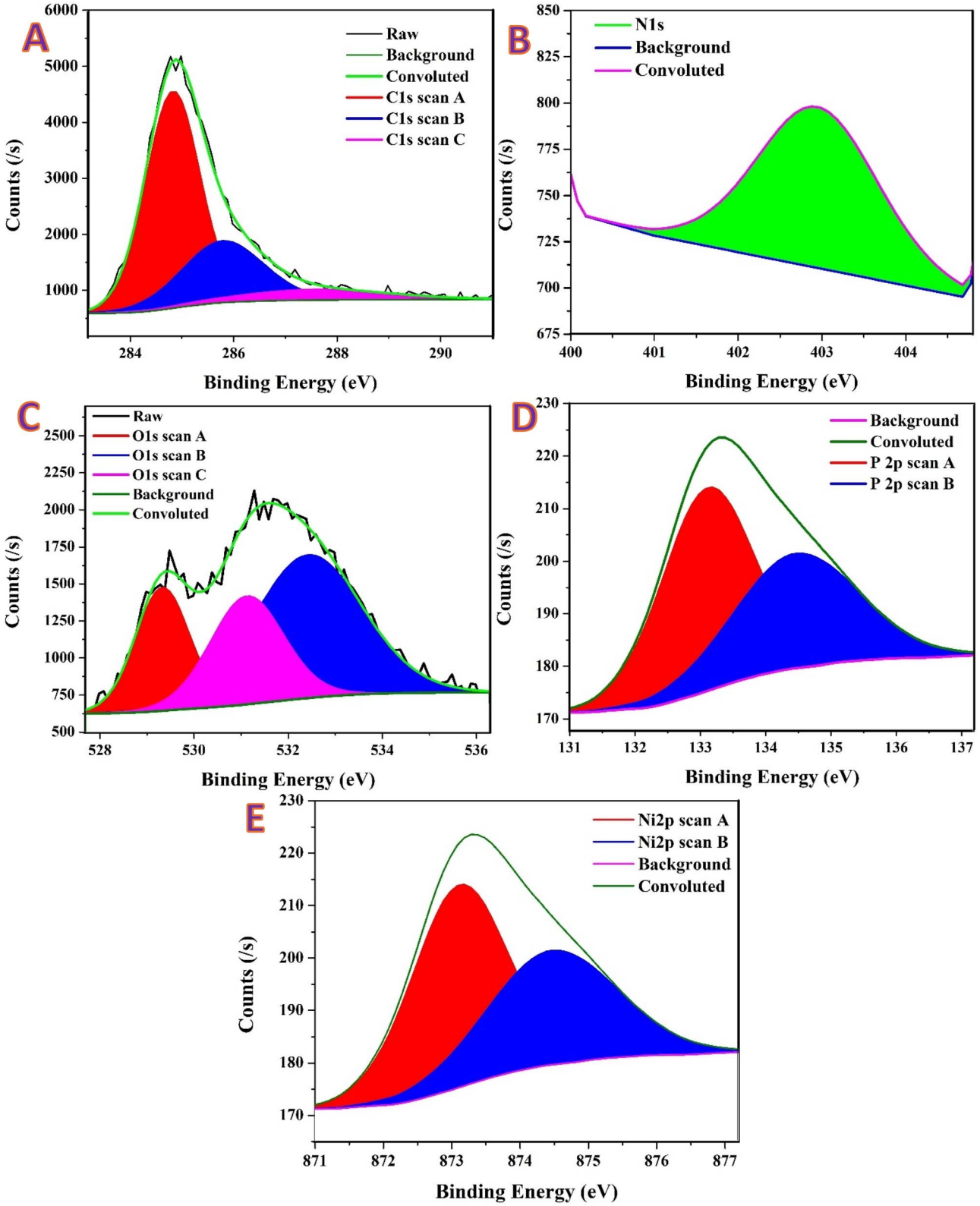

Fig. 4 XPS spectra of mono-ammonium-phosphate (MAP)-incorporated Ni/CNFs. Panels: (A) C 1s, (B) N 1s, (C) O 1s, (D) P 2p and (E) Ni 2p.

1.65 eV, area 68.9 CPS eV, 70.21%) and P $2p_{1/2}$ = 134.67 eV (FWHM 2.24 eV, area 29.2 CPS eV, 29.79%), with a spin–orbit separation of 1.56 eV and an area ratio close to the expected ~2 : 1. No intensity appears at 129–131 eV, ruling out phosphide (Ni_2P) or elemental P. The P 2p and O 1s assignments together indicate a thin, likely amorphous phosphate residue at the surface, in agreement with XRD which shows no crystalline phosphate phase.[35]

The Ni envelope (Fig. 4E) displays the characteristic mixture of oxidized states and shake-up satellites expected for air-exposed Ni nanoparticles. The principal Ni^{2+} lines appear at $2p_{3/2}$ = 853.85 eV (FWHM 1.54 eV, area 1094.2 CPS eV, 9.91%) and $2p_{1/2}$ = 871.88 eV (FWHM 2.73 eV, area 967.3 CPS eV, 8.92%). Ni^{3+} (NiOOH-like) contributions are observed at $2p_{3/2}$ = 856.10 eV (FWHM 3.37 eV, area 3482.9 CPS eV, 31.62%) and $2p_{1/2}$ = 873.97 eV (FWHM 2.60 eV, area 688.2 CPS eV, 6.36%). Intense satellites—860.95 eV (22.05%), 864.46 eV (7.96%), 876.95 eV (5.75%), and 880.17 eV (7.43%)—confirm a substantial Ni^{2+} fraction ($NiO/Ni(OH)_2$). Considering only the main lines, the surface Ni^{3+}/Ni^{2+} ratio is approximately 2.0; when the large Ni^{2+} satellite intensity is taken into account, the practical oxidation balance approaches ~1 : 1, *i.e.*, a mixed $NiO–Ni(OH)_2$/NiOOH shell. Any metallic Ni^0 signal (expected at ~852.6 eV in $2p_{3/2}$) is largely attenuated by this oxidized overlayer within the XPS probing depth (~5–7 nm), which is consistent with XRD/SAED showing metallic Ni in the bulk.

Quantitative XPS thus supports a Ni^0 core/$NiO_x(OH)_y$ shell anchored to a turbostratic, oxygen-functionalized carbon support, with phosphate present solely as surface PO_4 (P^{5+}). The carbon surface contains ~36% oxygenated functionalities (C–O/C═O), while oxygen is split roughly half-and-half between Ni-oxide/hydroxide species and carbon/adsorbate/phosphate contributions. This chemistry is entirely consistent with the synthesis pathway (phosphate-assisted nucleation followed by reduction during calcination) and with the structural data (XRD/TEM). From a functional standpoint, the $NiO_x/Ni(OH)_2$–NiOOH shell constitutes the known redox-active surface for alkaline electrocatalysis, whereas oxygenated carbon and phosphate groups enhance wettability and may provide P–O–Ni/P–O–C linkages that stabilize Ni nanoparticles against migration and sintering during operation.

Fig. 5 shows XPS results for the DAP-incorporated Ni/CNFs. As shown, the C 1s envelope (Fig. 5A) is deconvoluted into three components. The dominant peak at 284.76 eV (FWHM 1.26 eV, area 11 238.6 CPS eV) contributes 69.43% and corresponds to sp^2/sp^3 C–C/C–H from the PVA-derived turbostratic carbon. Oxygenated carbon appears as C–O/C–O–C (±C–N) at 286.05 eV (FWHM 2.05 eV, 23.80%, area 3849.1 CPS eV) and carbonyl/carboxylate (C═O/O–C═O) at 288.30 eV (FWHM 2.88 eV, 6.77%, area 1094.1 CPS eV). Compare to MAP (Fig. 4A) contains 36.0% oxygenated carbon (27.49% C–O; 8.49% C═O), whereas DAP shows 30.6%, *i.e.*, less oxygenated surface carbon. The oxygenated peaks in DAP are slightly upshifted (+0.26 eV for C–O and +0.70 eV for C═O), consistent with a somewhat different local chemical/charging environment expected for the more heavily decorated, inorganic-rich DAP surface seen in TEM. The larger non-oxygenated carbon fraction in DAP indicates that a greater portion of the outer surface is covered by metallic/oxide particles and phosphate rather than by highly functionalized carbon.

Fig. 5B demonstrates a single component centered at ~403 eV for N 1s (overlapping the total fit) is observed and assigned to oxidized/positively charged nitrogen ($N–O/N^+–O^-$). There is no resolvable intensity in the 397–400 eV range (no nitride or graphitic/pyridinic N). Comparison to MAP (Fig. 4B), identical behavior (MAP peak at 402.94 eV, FWHM 1.71 eV). Nitrogen therefore remains as only a trace oxidized residue in both materials after calcination.

Two oxygen environments are required for DAP (Fig. 5C), 531.14 eV (FWHM 1.45 eV, area 1417.6 CPS eV, 22.58%) attributed to hydroxyl/defect oxygen (Ni–OH/NiOOH) together with non-bridging phosphate oxygen (P═O/P–O^-), and 532.36 eV (FWHM 2.56 eV, area 4856.1 CPS eV, 77.42%) assigned to C–O–/O–C═O in carbon, molecular H_2O/adsorbates, and bridging P–O–M/P–O–C.[36] Notably, there is no resolved lattice O^{2-} peak at ~529.3 eV in DAP. MAP clearly displays three components with 21.93% lattice Ni–O–Ni at 529.33 eV, 26.22% hydroxyl/defect ± P═O at ~531.1 eV, and 51.84% carbon/adsorbate/bridging oxygen at ~532.4 eV. The DAP spectrum is therefore shifted toward higher-BE oxygen and lacks the distinct lattice-O^{2-} signature, indicating that DAP exposes a more hydrated/ligand-rich overlayer (hydroxyl, phosphate, carbon–oxygen, and H_2O) that attenuates the lattice oxide signal from the near-surface Ni.

As illustrated in the spectra of P 2p (Fig. 5D), DAP shows two peaks at 132.71 eV (11.56%) and 133.29 eV (88.44%), both within the P^{5+} phosphate range. The envelope is dominated by the ~133.3 eV component commonly associated with PO_4 bound to metals or carbon (P–O–Ni/P–O–C) in a hydrated environment. There is no low-BE signal (129–131 eV), ruling out phosphide. However, MAP displays a classic phosphate doublet at 133.11/134.67 eV (2 : 1 character). The slight lower BE and more asymmetric distribution in DAP are compatible with stronger coordination/hydration of phosphate at the surface of the more ligand-rich DAP fibers.

The DAP Ni 2p spectrum (Fig. 5E) shows a pronounced oxidized shell with enriched Ni^{3+} and a small metallic contribution: Ni^{3+} $2p_{3/2}$ at 856.05 eV (FWHM 3.37 eV, area 3089.5 CPS eV, 39.18%) and Ni^{3+} $2p_{1/2}$ at 873.23 eV (16.63%). A metallic Ni^0 $2p_{3/2}$ component is also resolved at 852.88 eV (FWHM 1.31 eV, 5.15%), consistent with large Ni cores, while the Ni^{2+} multiplet satellites are intense at 861.31 eV (21.80%), 865.39 eV (5.28%), 876.72 eV (5.23%), and 881.11 eV (4.70%) (total satellites ≈39%). Comparison to MAP (Fig. 4E): MAP contains Ni^{3+} $2p_{3/2}$ = 31.62% (856.10 eV), Ni^{2+} $2p_{3/2}$ = 9.91% (853.85 eV) with strong satellites (total ≈43%) and no resolvable Ni^0. DAP therefore exhibits more Ni^{3+} at the surface and reveals a small Ni^0 core signal, while its satellite fraction is slightly lower. Together with O 1s, this points to Ni^0 cores coated by a more NiOOH-rich, hydrated shell in DAP, whereas MAP retains a thinner oxide where lattice Ni–O is still detectable.[37]

Overall, the XPS results concluded that moving from MAP → DAP, the surface chemistry becomes (i) less carbon-oxygenated (C 1s), (ii) chemically similar in nitrogen (trace oxidized N only), (iii) dominated by hydroxyl/adsorbate/phosphate oxygen with no resolved lattice O^{2-} (O 1s), and (iv) more Ni^{3+}-rich with a detectable Ni^0 core signal (Ni 2p). Phosphorus remains P^{5+} (PO_4) in both, with DAP showing a slightly lower BE consistent with enhanced P–O–Ni/C coordination and hydration. This quantitative XPS picture agrees with the microscopy: DAP produces rougher fibers with heavier inorganic decoration, yielding Ni^0 cores wrapped by a thicker, NiOOH-rich and phosphate/adsorbate-laden shell, whereas MAP retains

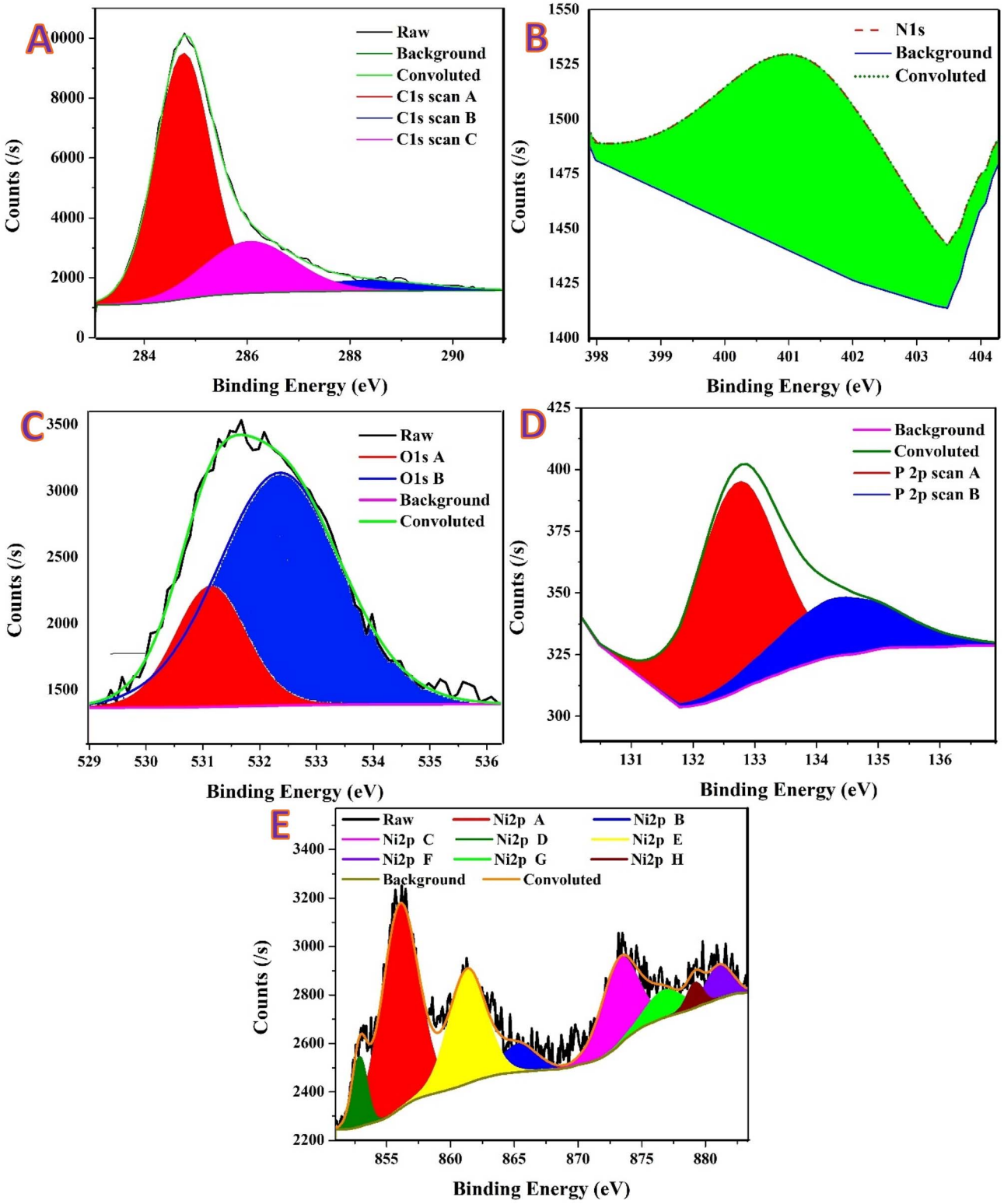

Fig. 5 XPS spectra of di-ammonium-phosphate (DAP)-incorporated Ni/CNFs. Panels: (A) C 1s, (B) N 1s, (C) O 1s, (D) P 2p and (E) Ni 2p.

a thinner oxide where lattice Ni–O is still visible. This distinction is expected to influence electrochemical behavior, with DAP surfaces primed for rapid $Ni(OH)_2$/NiOOH redox activation, and MAP offering a cleaner oxide/carbon balance with more evident lattice-oxide contribution.

3.1 Electrochemical activity

3.1.1 Electrochemical surface area. The activation of Ni-based electrocatalysts in alkaline media occurs *via* the surface redox transition between $Ni(OH)_2$ and NiOOH. When the

catalyst is cycled in alkaline solution (*e.g.* 1.0 M KOH) anodic polarization induces the oxidation of Ni(II) hydroxide to Ni(III) oxyhydroxide according to ref. 38:

$$Ni(OH)_2 \rightleftharpoons NiOOH + H^+ + e^- \quad (7)$$

During the reverse sweep, the NiOOH species are reduced back to $Ni(OH)_2$. These redox processes appear as characteristic peaks in the cyclic voltammogram (CV) and reflect the formation of the catalytically active NiOOH layer. The dynamic generation of this layer is crucial for alcohol electrooxidation, since NiOOH is widely recognized as the true active phase that mediates the dehydrogenation of glycerol and other polyols.[39]

The extent of Ni activation can be quantified by calculating the electrochemically active surface area (ECSA), which measures the number of redox-accessible Ni sites available for catalysis. ECSA is determined by integrating the charge under the Ni(II)/Ni(III) redox peaks and normalizing by the catalyst mass or electrode area. A higher ECSA indicates a larger population of accessible active sites, which directly correlates with greater catalytic activity. Thus, ECSA not only provides insight into the structural features of the catalyst (particle size, dispersion, accessibility) but also serves as a predictive descriptor for electrocatalytic performance. The electrochemically active surface area (ECSA) for the three formulations was estimated from the anodic Ni^{2+} Ni^{3+} charge using following equation:[40]

$$ECSA = \frac{1}{m \times q \times v} \int_{E_1}^{E_2} (j_{anode} - j_{baseline}) dE \quad (8)$$

where m is the mass of functional material, $v = 0.05$ V s^{-1}, j is the current, E is the applied potential and is the charge density range for $Ni(OH)_2$/NiOOH (~0.39 mC cm^{-2}).

Fig. 6A shows the CV responses of the prepared nanofibers with different DAP contents in 1.0 M KOH. The bare Ni-CNFs (0 wt% DAP) display only small redox peaks, reflecting limited activation and a modest population of NiOOH species. Incorporation of phosphate markedly enhances the intensity of the Ni(II)/Ni(III) redox couple, with the strongest peaks observed for the 7 wt% DAP sample. The calculated ECSAs were 6975, 9939, 33 103, 30 813, 40 600 and 2988 cm^2 g^{-1} for the nanofibers prepared from electrospun solution having 0, 1, 3, 5, 7 and 10 wt% DAP, respectively.

The data clearly reveal that phosphate incorporation strongly promotes the activation of Ni sites. In particular, the 7 wt% DAP formulation exhibits the highest ECSA, nearly six times greater than the phosphate-free sample. This enhancement is attributed to the favorable balance between Ni nanoparticle dispersion and the conductive, graphitized carbon framework observed in TEM/HRTEM analyses. At this composition, phosphate-derived functionalities likely stabilize Ni nanoparticles against excessive aggregation while simultaneously promoting the accessibility of surface hydroxyl groups, thereby facilitating the $Ni(OH)_2$/NiOOH redox transition.

The XPS results (Fig. 5) corroborate the electrochemical activation data. The presence of surface phosphate groups and hydroxyl-rich oxygen environments enhances the $Ni(OH)_2$/NiOOH transition, yielding higher ECSA values for phosphate-modified samples. In particular, the 7 wt% DAP catalyst, which exhibited the highest ECSA (40 600 cm^2 g^{-1}), benefits from an optimal balance: phosphate-derived groups increase OH^- affinity, graphitized carbon ensures high conductivity, and Ni nanoparticles provide abundant redox-active centers. Conversely, at 10 wt% DAP, the relative Ni surface contribution is diminished due to particle agglomeration and possible surface passivation by excess phosphate, consistent with the reduced ECSA and weaker CV response. These surface characteristics directly translate to enhanced glycerol electrooxidation, as catalysts with higher ECSA and optimized surface chemistry

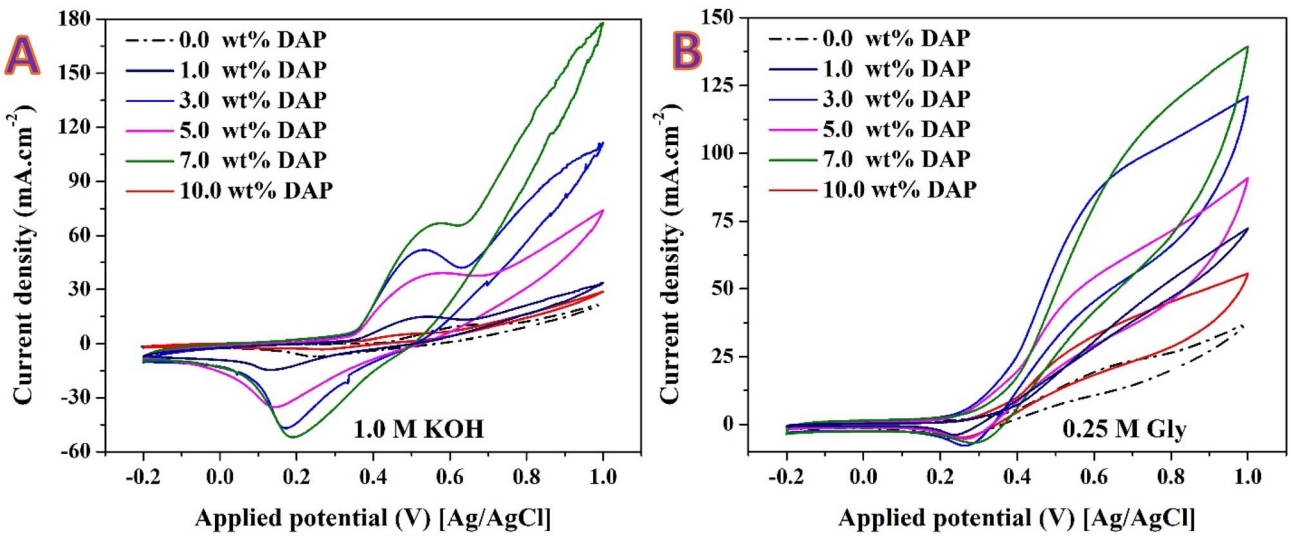

Fig. 6 Cyclic voltammetry (CV) of di-ammonium phosphate (DAP)-derived Ni-CNFs in 1.0 M KOH. (A) Activation profiles of nanofibers prepared with different DAP contents (0–10 wt%). (B) Electrocatalytic glycerin oxidation (0.25 M glycerin in 1.0 M KOH), where the current density trends follow the ECSA results.

expose more NiOOH sites, thereby accelerating the dehydrogenation steps of glycerol.

The voltammetric responses in glycerin-containing electrolyte (Fig. 6B) follow the canonical NiOOH-mediated pathway. Upon anodic polarization, surface $Ni(OH)_2$ is oxidized to NiOOH (vide Fig. 6A). The NiOOH layer acts as the true active phase, abstracting hydrogen from adsorbed glycerol to generate carbonyl/alcohol intermediates and subsequently higher-oxidized products; the catalytic cycle is closed by re-hydroxylation of reduced Ni sites by OH^-. Accordingly, catalysts that form more NiOOH (higher ECSA) should deliver earlier onset and larger oxidation currents in glycerin—exactly the trend observed here.

Relative to the phosphate-free control, all DAP-modified nanofibers display: a negative shift in onset potential for glycerin oxidation (earlier activation), a steeper current rise beyond ~0.55–0.65 V *vs.* Ag/AgCl, and substantially higher peak currents by 0.9–1.1 V. The activity ranks 7 wt% DAP > 3 wt% ≈ 1 wt% > 5 wt% ≫ 10 wt% ≳ 0 wt%, mirroring the ECSA order. The 7 wt% DAP electrode exhibits the highest current density across the whole potential window, reflecting the largest population of accessible NiOOH sites (ECSA ≈ 40 600 $cm^2\ g^{-1}$). Both 1 wt% and 3 wt% DAP show pronounced activity gains over the undoped sample, while 5 wt% remains intermediate. In contrast, 10 wt% DAP underperforms despite containing phosphate: its muted current and more positive onset are consistent with the very low ECSA (≈2988 $cm^2\ g^{-1}$), likely due to particle coarsening and partial surface passivation by excess phosphate residues that hinder Ni(II) → Ni(III) conversion and/or block glycerolate adsorption.

TEM/HRTEM revealed that DAP promotes Ni nanoparticle anchoring within a highly graphitized CNF matrix, improving electronic transport. At the optimal 7 wt%, this conductivity benefit coincides with a high density of redox-addressable Ni sites, enabling rapid NiOOH formation and turnover. Phosphate groups detected by XPS likely enhance surface hydrophilicity/OH^- affinity, and electronically tune Ni centers (together with the hydroxyl-rich O 1s component), lowering the barrier for the Ni(II) → Ni(III) step. These surface effects rationalize the earlier onset and larger kinetic currents observed for 1–7 wt% DAP.

The broad current growth rather than a sharp single peak is characteristic of mixed kinetic/mass-transport control in polyol oxidation on NiOOH, where multiple parallel oxidation routes (primary/secondary alcohol dehydrogenation, C–C bond scission at higher potentials) contribute. The steeper slope for 7 wt% suggests faster charge-transfer kinetics and higher site density, whereas curvature damping at 10 wt% indicates site scarcity and possibly product-adsorbate coverage at elevated potentials.

The glycerin CVs confirm that accessible NiOOH site density (ECSA) is the dominant descriptor of activity in this system. Controlled phosphate incorporation optimizes that descriptor by balancing Ni particle dispersion with a conductive, graphitized support and favorable surface chemistry. Over-phosphatization (10 wt%) reverses these gains by reducing exposed Ni and impeding activation.

3.1.2 Glycerin electrooxidation. In alkaline media, glycerin is oxidized on NiOOH formed *in situ* from surface $Ni(OH)_2$. Thus, catalytic current scales with the density and accessibility of NiOOH sites (ECSA) and the supply/transport of glycerolate to these sites. Panels 7 A–7F show the response of each formulation to increasing Gly concentration (0 → 1.0 M in 1.0 M KOH).

As shown for all formulations, relative to the blank electrolyte (0 M glycerin (Gly), dash–dot curve), adding Gly introduces a new anodic current growing beyond ~0.55–0.65 V *vs.* Ag/AgCl, superimposed on the Ni(II)/Ni(III) waves—diagnostic of NiOOH-mediated alcohol oxidation. Moreover, from 0.05 → 0.25 → 0.5 M Gly the current increases strongly, indicating that in this range the reaction is reactant-concentration/kinetic-limited (apparent first-order dependence at low glycerin concentration). Going to 1.0 M Gly often produces smaller incremental gains or a drop in current, together with larger hysteresis between forward/backward scans, revealing the onset of mass-transport limitations and/or surface coverage by intermediates (*e.g.*, glycerates/adsorbed carbonyl fragments) that partially poison NiOOH.

For the DAP-free nanofibers (0 wt% DAP; Fig. 7A), currents are the smallest of the series. Raising glycerin concentration from 0.05 to 0.5 M boosts the anodic current (kinetic regime), but the response saturates by 1.0 M, consistent with a low ECSA and limited number of NiOOH sites. On the other hand, for the 1 wt% DAP nanofibers (Fig. 7B) marked improvement over 0 wt%: earlier onset and higher currents at all glycerin concentrations. The largest rise occurs up to 0.5 M, after which the curve at 1.0 M shows only modest additional current, indicating the approach to mixed kinetic/transport control. The deeper cathodic dip at low glycerin concentrations reflects faster NiOOH reduction and stronger interaction with adsorbed intermediates.

Fig. 7C shows the obtained results for the 3 wt% DAP nanofibers. As shown, the activity increases further; 0.5 M yields a pronounced current jump and the most favorable onset among the low-DAP samples. The high currents mirror the large ECSA (≈3.31×10^4 $cm^2\ g^{-1}$). At 1.0 M, the gain is diminished—site coverage and diffusion start to limit the rate. For 5 wt% DAP sample (Fig. 7D), intermediate performance is detected between 3% and 1%. The current continues to rise up to 0.5 M; at 1.0 M the curves broaden and the slope decreases, consistent with growing transport/coverage effects on a moderate-ECSA surface (≈3.08×10^4 $cm^2\ g^{-1}$).

For the best-performing catalyst (7 wt% DAP Fig. 7E), across all concentrations, in line with its maximum ECSA (≈4.06×10^4 $cm^2\ g^{-1}$) and highly graphitized/functionalized surface. Onset is most negative, and kinetic currents are highest from 0.25 to 1.0 M. The curve at 0.5 M is particularly steep—indicative of fast charge transfer on a dense population of NiOOH sites. At 1.0 M the increase persists but with reduced efficiency, pointing to transport/coverage limitations rather than site scarcity. However, for the 10 wt% DAP (Fig. 7F), currents are significantly lower at every glycerin concentration, tracking the very low ECSA (≈2.99×10^3 $cm^2\ g^{-1}$). Excess phosphate leads to larger Ni particles and partial surface passivation; consequently, both onset and slope are inferior and the system enters transport limitation at much smaller absolute currents.

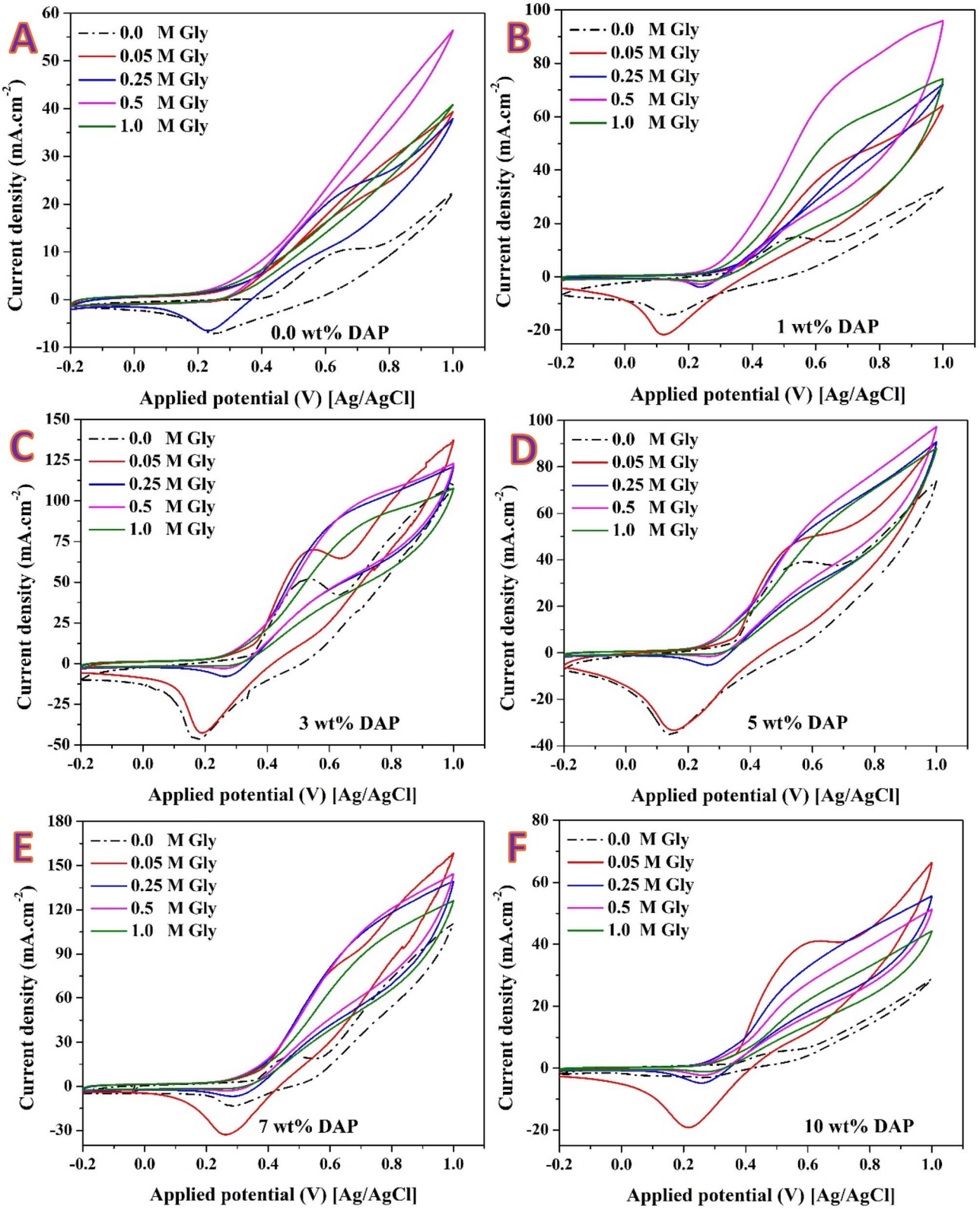

Fig. 7 Cyclic voltammetry curves of DAP-derived Ni-CNFs recorded in 1.0 M KOH with different glycerin concentrations. Panels correspond to nanofibers prepared with different DAP contents: (A) 0 wt%, (B) 1 wt%, (C) 3 wt%, (D) 5 wt%, (E) 7 wt%, and (F) 10 wt%.

Across all compositions, 0.5 M glycerin emerges as a practical optimum in the CV window, delivering the largest increases without severe mass-transport penalties. The activity ranking at each concentration follows the ECSA order confirming that accessible NiOOH site density is the dominant descriptor. The XPS-identified phosphate groups (P $2p_{3/2}$ ≈

134.2 eV) and hydroxyl-rich O 1s environment likely enhance OH^- affinity and facilitate Ni(II) → Ni(III) conversion, while the graphitized CNF backbone ensures rapid electron transport—together yielding the high kinetic currents of the 1–7% DAP catalysts, with a maximum at 7%. In contrast, over-phosphatization (10%) reduces exposed Ni and slows activation, so increasing glycerin concentration cannot compensate.

Fig. 8A compares the electrochemical performance of pristine Ni-CNFs (0 wt% ammonium phosphate) with those prepared using mono-ammonium phosphate (MAP) and di-ammonium phosphate (DAP). Both MAP- and DAP-derived catalysts exhibit substantially higher glycerin oxidation currents relative to the phosphate-free control, confirming that phosphate addition is crucial for improving Ni activation and catalytic utilization. Between the two, DAP-based nanofibers deliver higher current densities and a more favorable onset potential than MAP, consistent with the higher ECSA values observed for DAP formulations. This performance difference is explained by their distinct surface chemistries, as revealed by XPS.

Quantitative XPS of the MAP nanofibers showed a Ni^0 core/$NiO_x(OH)_y$ shell anchored to a turbostratic, oxygen-functionalized carbon support, with phosphate present solely as surface PO_4^{3-} (P^{5+}). The carbon contained ~36% oxygenated functionalities (C–O/C=O), while oxygen was split roughly evenly between Ni oxide/hydroxide and carbon/adsorbate contributions. This configuration provides a moderate density of redox-active sites and a hydrophilic, defect-rich carbon scaffold to stabilize Ni particles.

In contrast, XPS of DAP-derived nanofibers revealed a lower overall Ni surface fraction (2.6 at%) but enriched hydroxyl-rich O 1s (~531.5 eV) species and PO_4^{3-} at ~134 eV, strongly increasing OH^- affinity. The C 1s was dominated by sp^2 carbon (80% surface carbon), reflecting a more graphitized matrix. Together, this chemistry favors both conductivity (graphitized carbon) and surface redox kinetics (phosphate- and hydroxyl-functionalized Ni), enabling easier Ni(II) → Ni(III) transition. This explains why DAP nanofibers exhibit higher ECSA and superior glycerin oxidation activity compared to MAP nanofibers, despite MAP retaining a higher proportion of oxygenated carbon groups.

Thus, the difference between MAP and DAP is essentially one of surface chemistry tuning: MAP favors defect-rich carbon and moderate Ni–OH coverage, while DAP optimizes Ni redox accessibility and conductivity through graphitization and phosphate-derived surface chemistry. The result is enhanced NiOOH generation and catalytic activity in DAP.

Fig. 8B shows the effect of glycerin concentration (0–1.0 M) on the electrochemical response of MAP-based nanofibers. The catalytic current increases as glycerin concentration rises from 0.05 to 0.5 M, reflecting the availability of NiOOH sites formed during activation. At 0.25–0.5 M, the current increase is most significant, suggesting that this range provides an optimal balance between substrate availability and efficient site utilization. At 1.0 M glycerin, however, the current increase plateaus, and broader peaks appear, indicative of mass-transport limitations and surface coverage by intermediates that slow down the NiOOH regeneration cycle.

Compared to the DAP-based catalysts, the MAP nanofibers show lower peak currents and less steep anodic slopes at each glycerin concentration. This aligns with their lower ECSA (from Ni redox charge) and with the XPS evidence of fewer hydroxyl surface groups, which are crucial for NiOOH-mediated polyol oxidation. Although MAP nanofibers benefit from oxygenated carbon functionalities that enhance hydrophilicity and stabilize dispersion, they lack the combination of graphitized conductivity and phosphate-enriched surface chemistry found in DAP nanofibers.

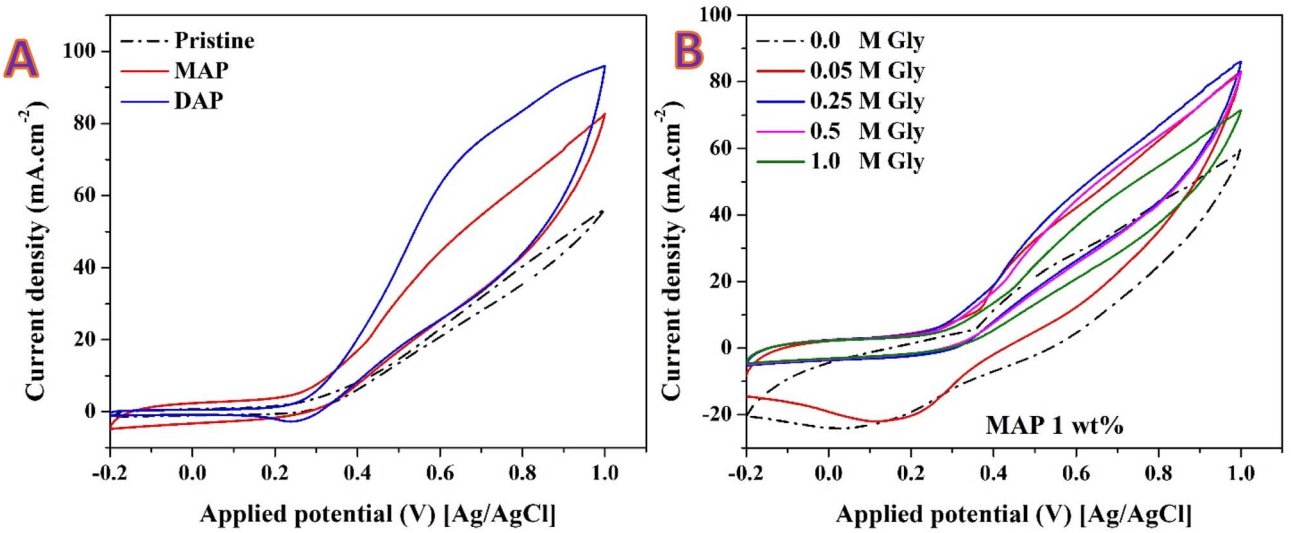

Fig. 8 Comparison of ammonium phosphate compositions in Ni-CNFs. (A) Cyclic voltammetry (CV) responses of pristine Ni-CNFs (0 wt% phosphate), mono-ammonium phosphate (MAP)-based nanofibers, and di-ammonium phosphate (DAP)-based nanofibers in 1.0 M KOH with 0.25 M glycerin. (B) CV curves of MAP (1 wt%) nanofibers at different glycerin concentrations (0.0–1.0 M) in 1.0 M KOH.

The results demonstrate that while both MAP and DAP improve Ni–CNF catalytic performance compared to phosphate-free samples, DAP nanofibers are superior due to their optimized balance of conductivity, Ni–OH redox accessibility, and phosphate-induced surface modifications. The concentration-dependent activity further emphasizes that the maximum efficiency is obtained at ~0.5 M glycerin, where the interplay of NiOOH formation, substrate availability, and mass transport is most favorable.

Fig. 8B (MAP 1 wt%) displays the CV response of the MAP-derived Ni-CNFs in 1.0 M KOH as the glycerin concentration is increased from 0 to 1.0 M. As expected for Ni catalysts in alkaline media, glycerin oxidation proceeds on NiOOH generated *in situ* from $Ni(OH)_2$; therefore, activity reflects (i) how readily the surface undergoes the Ni(II) → Ni(III) transition and (ii) the supply/transport of glycerolate to those sites.

Relative to the blank (0.0 M Gly, dash–dot), adding glycerin causes an anodic current to emerge beyond ~0.55–0.65 V *vs.* Ag/AgCl, characteristic of NiOOH-mediated oxidation. From 0.05 → 0.25 → 0.5 M, the current increases steadily and the slope of the forward scan becomes steeper, indicating that in this concentration window the reaction is primarily kinetically/concentration controlled; more substrate leads to higher site turnover on the available NiOOH.

Raising glycerin to 1.0 M does not yield a proportional current gain and the curves broaden (larger hysteresis between forward and reverse scans). This behavior points to mixed kinetic/transport control with partial surface coverage by intermediates (glycerates/carbonyl fragments) that temporarily block NiOOH and slow its regeneration—effects commonly observed for polyol oxidation on Ni.

XPS for MAP showed a Ni^0 core/$NiO_x(OH)_y$ shell on a turbostratic, oxygen-functionalized carbon support, with phosphate present as surface PO_4^{3-} (P^{5+}) and the carbon surface containing ~36% oxygenated groups (C–O/C=O). This chemistry renders the surface hydrophilic and stabilizes Ni nanoparticles, enabling clear Ni(II)/Ni(III) redox features and a tangible concentration dependence in glycerin. However, compared with DAP, MAP provides fewer hydroxyl-rich environments and less graphitized conductivity, so the density of redox-addressable Ni sites (ECSA) and the rate of NiOOH buildup are more modest.

At identical glycerin concentrations, DAP 1 wt% (Fig. 7B previously) exhibits earlier onset and higher currents than MAP 1 wt%, reflecting its larger ECSA and phosphate/–OH-enriched surface (P 2p ~134 eV; O 1s with a higher –OH fraction) together with a more graphitized CNF backbone. These attributes accelerate Ni(II) → Ni(III) activation and electron transport, giving DAP a steeper current rise from 0.25–0.5 M and better utilization of sites before mass-transport limitations appear. In contrast, MAP's oxygenated carbon (beneficial for wetting) does not compensate fully for its lower density of easily activatable Ni sites, so the activity—while clearly enhanced *versus* 0 M glycerin—remains below that of DAP.

For MAP 1 wt%, 0.5 M glycerin provides an effective balance: it maximizes the kinetic current without incurring the stronger transport/coverage penalties visible at 1.0 M. The same optimal concentration was observed for DAP catalysts, but absolute activity ranks DAP > MAP, consistent with the ECSA hierarchy and the XPS-derived surface chemistry differences. Overall, MAP (1 wt%) nanofibers show the expected concentration-dependent enhancement in glycerin oxidation, governed by NiOOH formation and substrate availability. Nevertheless, DAP counterparts outperform MAP at each concentration because phosphate-induced surface –OH enrichment and higher graphitization promote faster Ni activation and charge transfer, yielding a higher population of active NiOOH sites and, consequently, larger catalytic currents.

3.1.3 Electrooxidation reaction parameters. The influence of temperature (30–60 °C) on the electrocatalytic oxidation of glycerin by the 1 wt% DAP nanofibers in 0.25 M glycerin + 1.0 M KOH is presented in Fig. 9A. There is a clear enhancement of anodic current density with temperature with an increased slope in the forward scan. At 30 °C, the catalyst shows the expected NiOOH-mediated oxidation of glycerin with reasonable current density. Temperature elevation to 40 and 50 °C increases the anodic current, which is characteristic of enhanced reaction kinetics by improved adsorption of glycerolate, increased activation of OH^-, and enhanced charge transfer across the NiOOH/electrolyte interface. At 60 °C, maximum current density is achieved, and this indicates that the catalytic process possesses a good positive temperature dependence.

This effect can be explained by Arrhenius-type dependence of the reaction rate on temperature. High temperatures lower the activation barrier for dehydrogenation stages of glycerin oxidation and increase ionic conductivity of the electrolyte. Furthermore, the excess thermal energy promotes regeneration of NiOOH from $Ni(OH)_2$ and provides a greater number of active sites under repetitive potential cycling. The temperature rise in current density is also confirmed by earlier ECSA and XPS studies: the DAP nanofibers rich in phosphate reveal a high surface density of hydroxyl-rich Ni sites, and the increased thermal energy enhances their reactivity towards glycerin dehydrogenation. Interestingly, no apparent shift in onset potential is observed over the range tested, which means that the reaction pathway does not change, but the kinetics are accelerated. In sum, glycerin electro-oxidation on DAP nanofibers is strongly temperature dependent with consistently increasing activity between 30 and 60 °C. This observation accentuates the influence of thermal activation towards maximizing site utilization and highlights the potential of phosphate-modified Ni catalysts towards viable glycerin electrooxidation under modestly increased temperature.

To measure the temperature dependence quantitatively, an Arrhenius analysis was carried out by recording the anodic current at a fixed overpotential in the kinetic range (0.65–0.70 V *vs.* Ag/AgCl) for 30–60 °C. Linear fits of $\ln(i)$ *vs.* $1/T$ yielded an apparent activation energy of $E_a = 19 \pm 3$ kJ mol^{-1} for glycerin oxidation over the 1 wt% DAP nanofibers. The relatively low barrier is consistent with a NiOOH-promoted dehydrogenation mechanism aided by the phosphate-rich, hydroxyl-rich surface as determined by XPS and the highly graphitized CNF support (fast charge transfer). At larger overpotentials, the effective E_a is

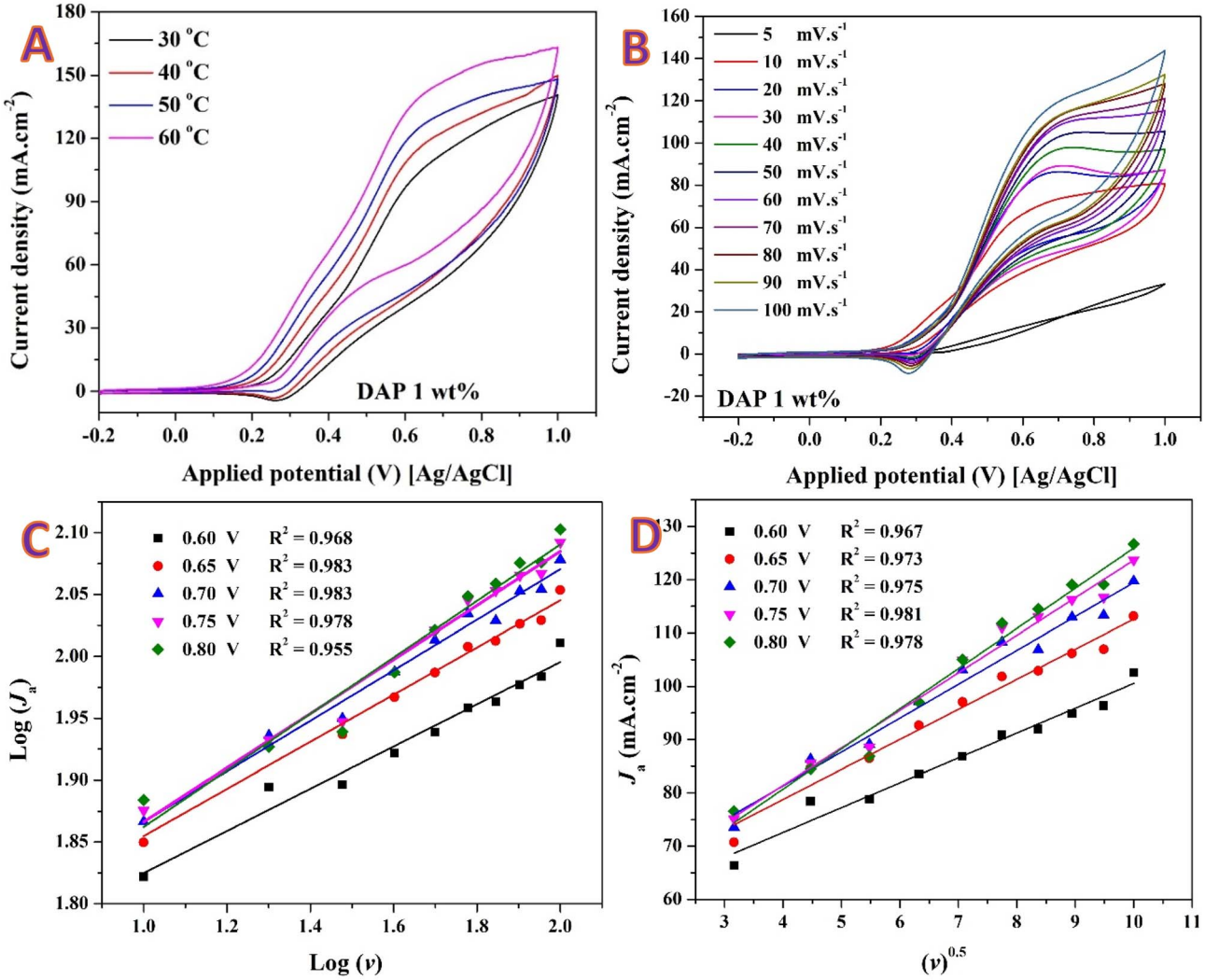

Fig. 9 Electrocatalytic behavior of 1 wt% DAP-derived Ni-CNFs toward glycerol oxidation in 1.0 M KOH: (A) effect of temperature; (B) scan-rate-dependent CVs (5–100 mV s^{-1}); (C) log(J_a)–log(v) plots (b = 0.17–0.23) indicating mixed control; and (D) linear J_a–$v^{1/2}$ relation confirming diffusion-influenced kinetics. Results reveal dominant diffusion contribution (~60–67%) in the Ni(II)/Ni(III)-mediated glycerol oxidation process.

diminished by mass-transport/coverage effects decreasing the intrinsic kinetic component, further indicating the need to evaluate E_a under conditions of kinetics. Overall, the observed activation energy confirms that the surface chemistry applied by DAP effectively lowers the energetic cost of the rate-determining steps, as is in line with the strong temperature-strengthened currents observed in Fig. 9A.

Cyclic voltammetry at variable scan rates is a classical diagnostic for probing the rate-determining steps of electrochemical and electrocatalytic systems. In a purely diffusion-controlled process, the peak current (J_a) scales with the square root of the scan rate ($v^{1/2}$) according to the Randles–Ševčík relationship, while for a surface-confined or capacitive process J_a increases linearly with v.[41] In complex catalytic systems such as the $Ni(OH)_2$/NiOOH–glycerol couple, the overall current response reflects a convolution of three contributions: (i) the electron-transfer kinetics of the Ni(II)/Ni(III) redox transition, (ii) the subsequent chemical oxidation of glycerol by NiOOH (an EC′ mechanism), and (iii) the transport of both hydroxide ions and glycerolate species through the electrolyte and porous catalyst layer. Hence, deviations from these ideal dependencies provide insight into whether the observed current is limited by charge-transfer, chemical, or mass-transport phenomena.[42]

Fig. 9B presents the cyclic voltammograms of the 1 wt% DAP-based Ni-CNF electrode recorded at scan rates between 5 and 100 mV s^{-1} in 0.25 M glycerol + 1.0 M KOH. The anodic current density increases progressively with v, while the onset potential remains essentially constant, indicating that the catalytic pathway is unchanged. At faster scans, the anodic and cathodic branches become more separated, evidencing increasing polarization losses and incomplete regeneration of NiOOH within the time scale of each potential sweep. This behavior already suggests that the process is not governed solely by surface kinetics but involves significant diffusion and surface-coverage effects.

The relationship between the logarithm of current density (J_a) and the logarithm of the scan rate follows $J_a = a \times v^b$. The slopes extracted at various potentials (0.60–0.80 V) yield b =

0.17–0.23 ($R^2 \geq 0.96$), substantially lower than the theoretical limits for either diffusion control ($b = 0.5$) or surface control ($b = 1.0$). Such small exponents indicate a mixed-controlled regime dominated by mass-transport and coverage effects rather than intrinsic electron-transfer kinetics.[43] Specifically, as the potential sweep accelerates, the formation of intermediate glycerolate or carbonyl species on the NiOOH surface partially blocks active sites, reducing the number of accessible Ni^{3+} centers that can participate in the oxidative cycle. Concurrently, transport of hydroxide and glycerol molecules through the porous carbon nanofiber network and to the Ni sites becomes rate-limiting.

Plotting the anodic current density against the square root of the scan rate (Fig. 9D) produces nearly linear relationships ($R^2 \approx 0.97$–0.98) across the entire potential window, with slopes increasing from 4.66 to 7.53 mA cm^{-2} (mV $s^{-1})^{-1/2}$ as the potential increases from 0.60 to 0.80 V. This linearity demonstrates that the overall current is proportional to $v^{1/2}$, confirming that the oxidation reaction is diffusion-influenced under the tested conditions.[44] The mixed-control fitting $J_a = k_1 \times v + k_2 \times v^{1/2}$ further quantifies this behavior: the diffusion-related term ($v^{1/2}$) contributes approximately 60–67% of the total current at a representative 50 mV s^{-1}, while the surface-controlled fraction ($k_2 \times v^{1/2}$) remains minor. The dominance of the diffusion term supports the interpretation of an EC′ mechanism where NiOOH acts as a redox mediator whose regeneration is partially hindered by species transport within the electrode microstructure.

The electrochemical response of the 1 wt% DAP nanofibers is consistent with their structural and surface features revealed by XRD, TEM, and XPS. XRD and SAED confirmed the presence of metallic Ni with a face-centered cubic structure (major reflections at $2\theta \approx 44.8°$, 52.2°, 76.8°) embedded in a partially graphitized carbon matrix. HR-TEM images showed uniformly distributed Ni nanoparticles (≈40–60 nm) anchored within the conductive CNF network, and lattice fringes of 0.13 nm corresponded to the (220) plane of Ni, confirming strong metal–carbon coupling. Such morphology enhances electronic conductivity and mechanical integrity but simultaneously creates a hierarchically porous network, where diffusion of reactants through tortuous paths can become limiting during fast scans—exactly the behavior inferred from the low *b*-values.

The XPS spectra corroborate this interpretation: the surface of DAP-derived fibers contains Ni^{2+}/Ni^{3+} species (Ni $2p_{3/2} \approx 856.8$ eV), phosphate groups (P 2p ≈ 134 eV), and hydroxyl-rich oxygen species (O 1s ≈ 531.5 eV). These functional moieties increase hydrophilicity and OH^- adsorption, facilitating the formation of the active NiOOH layer. However, at high scan rates the rapid accumulation of adsorbed intermediates on these same hydroxyl-rich sites can temporarily suppress reoxidation kinetics, again producing the observed transport/coverage-controlled behavior.

The combined electrochemical and structural evidence reveals that glycerol oxidation on the DAP-derived Ni-CNFs proceeds *via* a Ni(II)/Ni(III) mediated dehydrogenation sequence, but under the tested dynamic conditions, the process is predominantly diffusion- and adsorption-limited. The low *b* values and strong $v^{1/2}$ scaling signify that further enhancement will depend more on mass-transfer engineering—thinner or more open fiber mats, convective flow, or elevated temperature (as evidenced in Fig. 9A)—than on additional intrinsic activation of the Ni centers. The robust linearity and reproducibility across potentials nevertheless confirm that the DAP modification provides a stable, uniformly active catalytic surface capable of sustaining the NiOOH–$Ni(OH)_2$ redox cycle even under high dynamic load.

3.1.4 Electrode stability. Fig. 10 presents the chronoamperometric (CA) profiles of the 1 wt% DAP-derived Ni-CNF electrode recorded at different applied potentials (0.4–0.7 V *vs.* Ag/AgCl) in 0.25 M glycerol + 1.0 M KOH. The electrode was subjected sequentially to each potential for 1000 s using the same working electrode under identical conditions to assess its catalytic stability and tolerance toward intermediate poisoning during glycerol oxidation.

In all cases, the current density initially exhibits a sharp decay within the first few seconds, followed by a steady-state region that persists over the remaining duration. The initial decay corresponds to the rapid double-layer charging and the accumulation of adsorbed reaction intermediates—such as glycerolate, carbonyl, and formate species—on the NiOOH catalytic sites.[34,45] Once equilibrium coverage is achieved, a balance is established between the formation and oxidation of these intermediates, leading to a quasi-stable current response. This behavior is typical of well-behaved Ni-based catalysts operating *via* a Ni(II)/Ni(III)-mediated EC′ mechanism, where NiOOH acts as the oxidizing agent and is continuously regenerated *in situ*.[46]

As the applied potential increases from 0.4 to 0.7 V, the steady-state current density systematically rises from approximately 15 to 60 mA cm^{-2}, reflecting the increased driving force for both $Ni(OH)_2$ oxidation and glycerol dehydrogenation. At higher potentials (0.6–0.7 V), the current stabilizes rapidly and maintains over 90% of its initial value after 1000 s, demonstrating excellent temporal stability and high tolerance toward

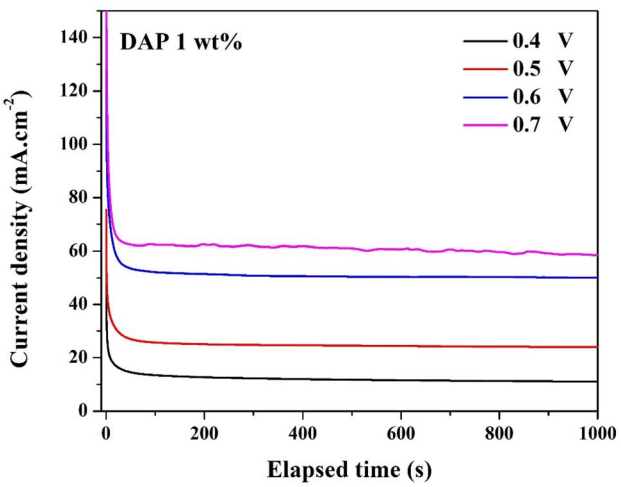

Fig. 10 Chronoamperometric response of 1 wt% DAP-derived Ni-CNFs in 0.25 M glycerol + 1.0 M KOH at various potentials (0.4–0.7 V *vs.* Ag/AgCl).

intermediate adsorption. This stability suggests that phosphate incorporation from DAP effectively modifies the local electronic and chemical environment of the Ni sites, preventing irreversible oxidation or accumulation of strongly bound intermediates that would otherwise deactivate the surface.

The remarkable stability can be directly related to the material's physicochemical features revealed by XRD, TEM, and XPS. XRD and TEM confirmed the coexistence of crystalline metallic Ni nanoparticles embedded within a partially graphitized carbon matrix. The strong Ni–C interfacial coupling ensures efficient charge transfer and mechanical robustness during potential cycling, mitigating structural degradation and agglomeration of active sites. XPS analysis revealed the presence of Ni^{2+}/Ni^{3+} redox pairs alongside surface phosphate (P^{5+}) and nitrogen functionalities. These dopants enhance electronic conductivity and introduce oxygenated and phosphate-rich coordination sites, which stabilize the NiOOH layer by moderating its local charge density and hydrophilicity. The phosphate groups also act as proton acceptors, facilitating the regeneration of NiOOH and minimizing surface fouling by intermediates. Together, these features create a synergistically stabilized active surface, capable of sustaining the $Ni(OH)_2$/NiOOH redox cycle over prolonged operation without deactivation. The ability of the same electrode to recover its activity across multiple potential steps indicates reversible surface dynamics and minimal morphological degradation, consistent with the homogeneous distribution of Ni and P species observed in the elemental mapping and the uniform nanofiber morphology from SEM/TEM analyses.

Although each chronoamperometric step was recorded for 1000 s, it should be emphasized that the measurements were conducted sequentially using the same anode electrode, by switching the applied potential every 1000 s (0.4–0.7 V). Therefore, the electrode experienced a cumulative operation time exceeding 4000 s under glycerol oxidation conditions, without replacement or surface renewal. Notably, this stability test was

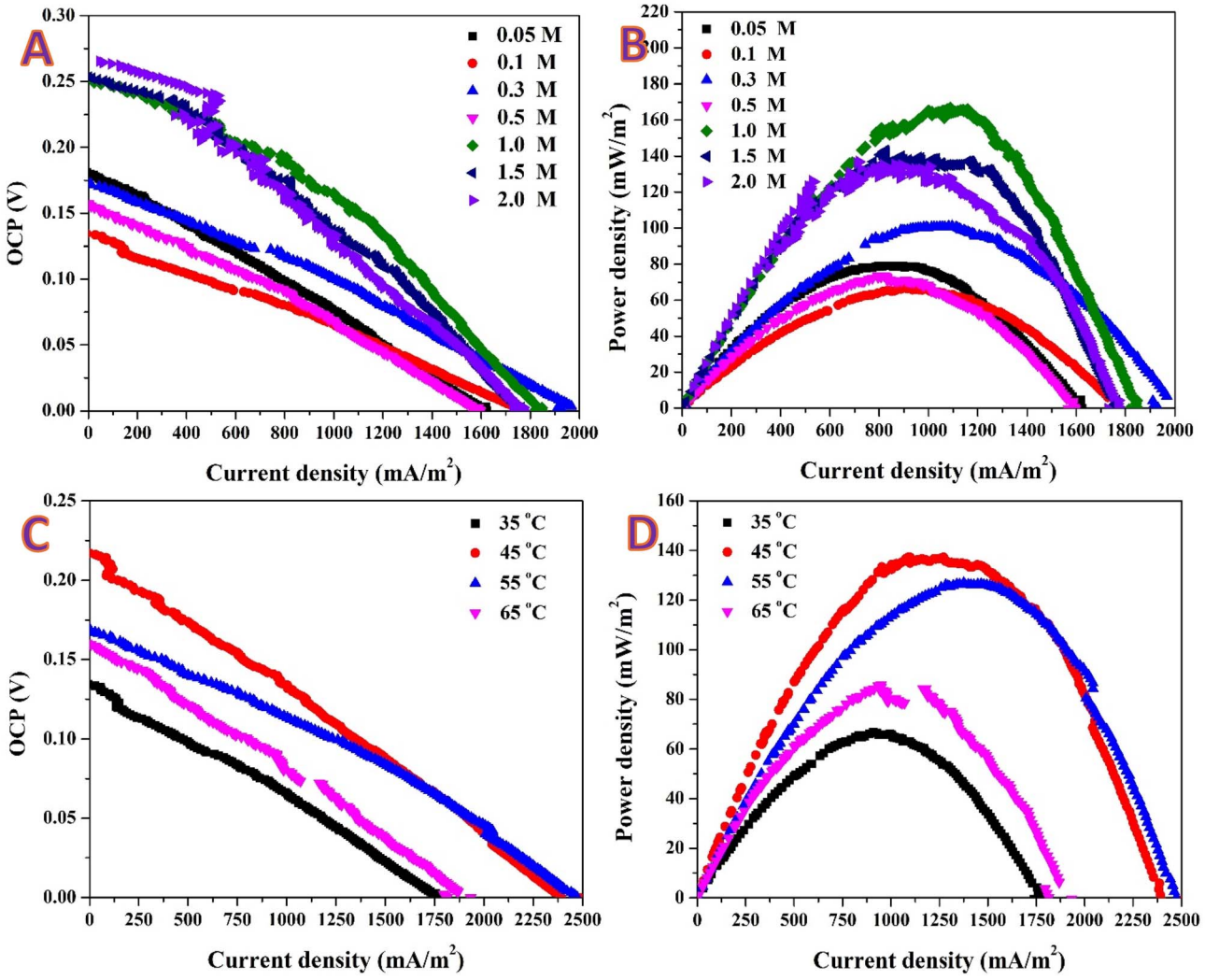

Fig. 11 (A) Polarization curves and (B) corresponding power density–current density plots for the direct glycerol fuel cell using 1 wt% DAP-derived Ni-CNFs as the anode at various glycerol concentrations in 1.0 M KOH. (C) Polarization and (D) power density–current density curves of a direct glycerol fuel cell using 1 wt% DAP-derived Ni-CNFs as the anode catalyst at different operating temperatures (35–65 °C) in 0.25 M glycerol + 1.0 M KOH.

performed after the electrode had already been subjected to extensive electrochemical evaluation (*e.g.*, cyclic voltammetry at different scan rates and concentration/temperature-dependent studies), meaning that the recorded steady-state current plateaus reflect the durability of a pre-activated and repeatedly stressed catalyst layer rather than a freshly prepared electrode.

3.2 Direct glycerol fuel cell (DGFC)

Fig. 11A shows the polarization (OCP–current density) plots of the direct glycerol fuel cell (DGFC) with the 1 wt% DAP-derived Ni-CNF as anode catalyst, evaluated at varied glycerol concentrations (0.05–2.0 M) in 1.0 M KOH. Fig. 11B displays the corresponding power density–current density plots under the same conditions. The systematic variation of glycerol concentration permits viewing of the connection between fuel availability, mass transport, and the intrinsic catalytic activity of the electrode.

Polarization curves exhibit a three-region profile as follows: (1) activation region at low current densities (0–400 mA m^{-2}), (2) ohmic region in which voltage decreases almost linearly with current density, and (3) mass transport region at larger currents, when fuel diffusion and product accumulation begin to limit performance. For low glycerol levels (≤0.1 M), OCP is in the range of 0.10–0.15 V, and current generation is fairly low based on a deficiency of fuel molecules that can reach active sites. OCP of the cell is increased by raising the glycerol level to ~0.25 V and enjoys significantly higher current density, indicative of improved reaction kinetics and fuel utilization efficiency. Such an improvement continues up to 1.0 M glycerol, followed by a smooth decline for 1.5 and 2.0 M solutions. The drop in voltage at higher concentrations most likely stems from increasing viscosity, bubble generation, and adsorption of oxidation intermediate species (*i.e.*, glycerate, glycolate, and carbonate species), which slow down mass transport and block the NiOOH active sites.

The optimal performance is obtained at 1.0 M glycerol, thus confirming this as the optimal compromise between sufficient fuel concentration and acceptable diffusion resistance. This concentration-dependent performance is in agreement with previous CV performance (Fig. 7 and 8), where the optimal anodic current density was also obtained at intermediate glycerol concentration. The OCP trend also supports the mixed kinetic-diffusion control mechanism shown above (Fig. 9), and the electrode exhibits a stable potential response during long-term operation. This stability also facilitates robust electronic coupling between the metallic Ni core and the graphitic carbon matrix, which ensures good charge transfer and maintains low internal resistance losses.

Current density–power density plots (Fig. 11B) are parabolic and typical of direct alcohol fuel cells. Power density increases with current until a maximum is reached, afterwards declining because of higher ohmic and mass-transport losses. The highest peak power density (~190–200 mW m^{-2}) was observed at all concentrations tested for the 1.0 M glycerol solution at a current density of approximately 1600–1700 mA m^{-2}. This improved performance at 1.0 M is attributed to: (1) tuned fuel concentration, which facilitates a higher availability of glycerol molecules to the NiOOH catalytic layer to sustain high-speed oxidation cycles; (2) high-performance Ni^{2+}/Ni^{3+} redox mediation, in which DAP doping facilitates the formation and regeneration of NiOOH as the main active species; (3) enhanced electron transportation, owing to the high-conductive and partially graphitized CNF network validated by TEM and XRD; (4) surface incorporation of phosphate, as confirmed by XPS, that creates electron-rich and hydrophilic environments favoring adsorption of OH^- and stabilizing operation condition surface interaction of Ni–O–P.

For more concentrated glycerol solutions (≥1.5 M), the power density reduces slightly (~160 mW m^{-2} at 2.0 M), in line with diffusion limitations and active site blockage by intermediate species. This trend reflects saturation of the catalytic surface, reducing the turnover frequency of NiOOH formation. However, the electrode is still fairly active under these concentrated solutions, which reflects its excellent tolerance against fuel crossover and poisoning by intermediates.

The 1 wt% DAP-derived electrode exhibits superior DGFC activity due to its synergistic physicochemical architecture: Ni nanoparticles are active catalytic sites, enabling efficient glycerol dehydrogenation through a $Ni(OH)_2$/NiOOH redox cycle. Phosphate dopants are surface stabilizers, preventing Ni oxidation to inactive NiO and enhancing OH^- adsorption kinetics. Nitrogen doping introduces defect sites and improves the electrical conductivity of the carbon matrix. Graphitic CNF support provides good mechanical stability and minimal charge-transfer resistance, with constant current output for extended periods of operation. Together, these attributes render a highly stable and electronically integrated catalyst system with efficient multi-electron oxidation of glycerol to C_3 intermediates and smaller products. The results conclusively demonstrate the superior electrocatalytic and operational performance of DAP-modified Ni-CNFs over undoped or MAP-based counterparts.

Fig. 11C illustrates the polarization characteristics, and Fig. 11D shows the corresponding power density–current density curves of the DGFC with the 1 wt% DAP-sourced Ni-CNF anode catalyst in 0.25 M glycerol + 1.0 M KOH at different working temperatures (35–65 °C). These measurements were collected to evaluate the influence of heat activation on the electrochemical reaction rate and overall energy conversion efficiency of the new anode material.

The polarization plots exhibit the typical negative slope with increasing current density, characteristic of activation-controlled, ohmic, and mass-transport-limited regimes in alkaline fuel cells. At 35 °C, the open-circuit potential (OCP) is approximately 0.12 V, and the current density is relatively low, which suggests slow charge-transfer kinetics and sluggish glycerol adsorption. Raising the temperature to 45 °C improves both the OCP and slope substantially and results in maximum performance with minimum voltage loss per unit current. The improvement arises due to enhanced reaction kinetics, improved mobility of hydroxide ions, and facile diffusion of glycerol molecules toward the active NiOOH sites.

At elevated temperatures (55–65 °C), the polarization curves experience less improvement, and at 65 °C, the voltage drops

slightly with rising current densities. The drop is the result of enhanced side reactions, such as overoxidation of Ni or electrolyte evaporation, and surface intermediate instability at high temperatures. These reactions can lead to partial deactivation of active NiOOH sites or increased cell internal resistance.

Temperature-dependent experiments yielded approximate activation energies of ~19 kJ mol^{-1} from CV currents in the kinetic regime (charge transfer mediated by NiOOH) and ~11 kJ mol^{-1} from Arrhenius analyses of the DGFC peak power density (whole-cell response including ohmic/transport contributions). Collectively, the average apparent barrier is ~15 ± 5 kJ mol^{-1}, as expected for an easy NiOOH-facilitated dehydrogenation process on the DAP-modified Ni-CNFs. The lowered device-level value factors in additional mass-transport contributions and internal resistance that account for some of the inherent kinetics.

The corresponding power density–current density plots exhibit parabolic profiles with well-defined maxima, which shift toward higher current densities as the temperature increases from 35 to 55 °C. The peak power density increases from ~80 mW m^{-2} at 35 °C to ~145 mW m^{-2} at 45 °C, and then saturates at ~140 mW m^{-2} at 55 °C. A moderate drop to ~120 mW m^{-2} occurs at 65 °C, consistent with the polarization data. The initial increase in power density with temperature is attributed to the temperature-activated nature of the redox transition $Ni(OH)_2$/NiOOH. Increased temperature increases the high-rate $Ni(OH)_2$-to-NiOOH transformation, the real active phase for glycerol electrooxidation. That is accompanied by larger charge-transfer rates (k_a) and smaller activation energy. The gradual drop-off above 55 °C suggests that the kinetic loss associated with catalyst deactivation and bubble stacking begins to predominate over the kinetic advantages, suggesting an optimal working range near 45–55 °C. The maximum power densities achieved and the trend with temperature parallel other alkaline direct alcohol fuel cells with Ni-anodes but are significantly higher in this instance involving the characteristic Ni–P–N synergy of the DAP-modified carbon nanofiber matrix.

The thermal response of the cell is intrinsically associated with the structural characteristics of the 1 wt% DAP-derived Ni-CNFs: (1) XPS analysis confirmed the occurrence of P^{5+} species of surface phosphate groups coordinating with Ni sites, stabilizing the NiOOH phase by regulating local charge density and inhibiting thermal oxidation to inactive NiO. (2) N incorporation improves defect-rich carbon structure, increasing electronic conductivity and offering stable electron mobility even at elevated temperatures.

TEM and XRD analysis revealed a metallic Ni core encapsulated by graphitic carbon, collectively forming a stable conductive network that permits structural stability upon repeated thermal stressing. These features combined ensure that the electrode remains stable and retains its catalytic activity to 55 °C without significant loss compared to undoped Ni/CNF systems, which are known to display significant deactivation by way of particle agglomeration or carbon corrosion.

The temperature-responsiveness highlights kinetic improvement over structural stability. At intermediate temperatures, enhanced OH^- mobility and fast Ni(II)/Ni(III) redox modifications dominate, allowing glycerol oxidation through subsequent C–H bond activation steps. At temperatures above 55 °C, however, overly extensive intermediate accumulation by the like of glycerate and formate species can perturb catalytic turnover and increase local pH gradients, causing somewhat diminished output. From an application point of view, the optimal operation window (45–55 °C) gives a good compromise between stability and performance, confirming the relevance of the DAP-Ni-CNF electrode to practical DGFCs under moderate conditions.

4 Conclusions

P,N-doped Ni-contained CNFs were successfully achieved by electrospinning and post-thermal treatment of nickel acetate and ammonium phosphate precursors. Structural and surface investigations revealed the achievement of a conductive, partially graphitized CNF network containing evenly dispersed Ni nanoparticles stabilized by phosphate and nitrogen functionalities. The nanofibers exhibited superior electrocatalytic activity toward glycerol oxidation in alkaline media, fueled by the Ni(II)/Ni(III) redox cycle forming highly active NiOOH sites. The 1 wt% DAP-nanofibers showed the best performance with a current density of ~140 mA cm^{-2}, an ECSA of ~40 600 cm^2 g^{-1}, and low activation energy of ~15 kJ mol^{-1}. In direct glycerol fuel cell operation, the electrode produced a peak power density of ~200 mW m^{-2}, demonstrating great electrochemical stability in continuous operation. The synergistic effect of P and N dopants improved redox reversibility, charge transfer, and resistance to intermediate poisoning. Besides their outstanding electrochemical performance, the P,N-doped Ni-CNFs offer a sustainable pathway to convert renewable electricity from glycerol, an inexpensive by-product of biodiesel production, into useful electricity. In this manner, this work combines waste-to-energy conversion, circular bioeconomy, and novel nanostructured catalyst engineering. The resulting Ni–P–N-CNFs thus constitute an optimal, durable, and sustainable anode platform for direct glycerol fuel cells and other emerging renewable energy devices.

Author contributions

Nasser A. M. Barakat: conceptualization; methodology; writing – original draft; supervision; project administration. Ahmed Saadawi: validation, data accusation, Shimaa Hamda: formal analysis, methodology.

Conflicts of interest

The authors declare no conflict of interest.

Data availability

All data generated or analyzed during this study are included in this published article.

Acknowledgements

The authors declare that no funding was received to support this study. During the preparation of this work, the authors used ChatGPT (OpenAI) to improve grammar, clarity, and language expression. The authors reviewed and edited the content and take full responsibility for the final publication.

References

1 D. Kour, K. L. Rana, N. Yadav, A. N. Yadav, A. A. Rastegari, C. Singh, P. Negi, K. Singh and A. K. Saxena, *Prospects of Renewable Bioprocessing in Future Energy Systems*, 2019, pp. 1–50.
2 M. V. Rodionova, R. S. Poudyal, I. Tiwari, R. A. Voloshin, S. K. Zharmukhamedov, H. G. Nam, B. K. Zayadan, B. D. Bruce, H. J. Hou and S. I. Allakhverdiev, *Int. J. Hydrogen Energy*, 2017, **42**, 8450–8461.
3 X. Fan, R. Burton and Y. Zhou, *Open Energy Fuels J.*, 2010, **3**, 17–22.
4 M. Hájek and F. Skopal, *Bioresour. Technol.*, 2010, **101**, 3242–3245.
5 F. Yang, M. A. Hanna and R. Sun, *Biotechnol. Biofuels*, 2012, **5**, 13.
6 B. Habibi, K. Farhadi and E. Minaie, *Int. J. Hydrogen Energy*, 2024, **91**, 1452–1462.
7 N. A. Barakat, S. Hamada, I. Mustafa and H. Alhumade, *Mater. Adv.*, 2025, **6**, 4538–4549.
8 E. Antolini, *Catalysts*, 2019, **9**, 980.
9 N. A. Barakat, A. Saadawi, K. Madih and R. Hefny, *Next Mater.*, 2025, **9**, 101036.
10 T. Li and D. A. Harrington, *ChemSusChem*, 2021, **14**, 1472–1495.
11 M. S. Houache, E. Cossar, S. Ntais and E. A. Baranova, *J. Power Sources*, 2018, **375**, 310–319.
12 P. A. Alaba, C. S. Lee, F. Abnisa, M. K. Aroua, P. Cognet, Y. Pérès and W. M. A. Wan Daud, *Rev. Chem. Eng.*, 2021, **37**, 779–811.
13 L. Fan, B. Liu, X. Liu, N. Senthilkumar, G. Wang and Z. Wen, *Energy Technol.*, 2021, **9**, 2000804.
14 H. Wang, J. Ding, P. Kannan, P. Subramanian and S. Ji, *Int. J. Hydrogen Energy*, 2020, **45**, 28821–28835.
15 R. S. Zakari, G. D. G. Peña, A. H. Pasanaje, M. Elsayed, S. Kuppireddy, M. I. H. Ali, A. Raj and M. Elkadi, *Case Stud. Chem. Environ. Eng.*, 2024, **10**, 100768.
16 V.-H. Do and J.-M. Lee, *Chem. Soc. Rev.*, 2024, **53**, 2693–2737.
17 Z. Zhao, H. Chen, W. Zhang, S. Yi, H. Chen, Z. Su, B. Niu, Y. Zhang and D. Long, *Mater. Adv.*, 2023, **4**, 835–867.
18 B. Wu, H. Meng, D. M. Morales, F. Zeng, J. Zhu, B. Wang, M. Risch, Z. J. Xu and T. Petit, *Adv. Funct. Mater.*, 2022, **32**, 2204137.
19 L. Zhang, A. Aboagye, A. Kelkar, C. Lai and H. Fong, *J. Mater. Sci.*, 2014, **49**, 463–480.
20 M. Li, Y. Liang, J. Shi, Q. Li, Q. Xu and W. B. Cai, *Chem. Rec.*, 2025, **25**, e202400240.
21 R. Rosei, S. Modesti, F. Sette, C. Quaresima, A. Savoia and P. Perfetti, *Phys. Rev. B: Condens. Matter Mater. Phys.*, 1984, **29**, 3416.
22 L. M. Moreau, D.-H. Ha, H. Zhang, R. Hovden, D. A. Muller and R. D. Robinson, *Chem. Mater.*, 2013, **25**, 2394–2403.
23 K. Rezapour, B. Habibi and H. Imanzadeh, *Int. J. Hydrogen Energy*, 2025, **184**, 151857.
24 J. C. De Jesus, I. González, A. Quevedo and T. Puerta, *J. Mol. Catal. A: Chem.*, 2005, **228**, 283–291.
25 N. A. Barakat, K. A. Khalil, I. H. Mahmoud, M. A. Kanjwal, F. A. Sheikh and H. Y. Kim, *J. Phys. Chem. C*, 2010, **114**, 15589–15593.
26 X. Wu, F. Yuan, M. Yang, P. Jiang, C. Zhang, L. Chen, Y. Wei and E. Ma, *Sci. Rep.*, 2015, **5**, 11728.
27 W. Shi, A.-H. Park, B. J. Cha, H.-U. Park, Y.-D. Kim and Y.-U. Kwon, *Appl. Surf. Sci.*, 2020, **504**, 144355.
28 G. S. Rellick and P. Adams, *Carbon*, 1994, **32**, 127–144.
29 X. Chen, X. Wang and D. Fang, *Fullerenes, Nanotubes Carbon Nanostruct.*, 2020, **28**, 1048–1058.
30 S. Yumitori, *J. Mater. Sci.*, 2000, **35**, 139–146.
31 T. Kato, Y. Yamada, Y. Nishikawa, T. Otomo, H. Sato and S. Sato, *J. Mater. Sci.*, 2021, **56**, 15798–15811.
32 S. Kobayashi, K. Miyazaki, S. Nozaki, H. Morisaki, S. Fukui and S. Masaki, *J. Vac. Sci. Technol., A*, 1996, **14**, 777–780.
33 H. Zhang, W. Wang, M. Chen and H. Wan, *Appl. Surf. Sci.*, 2018, **439**, 569–576.
34 N. A. Barakat, M. A. Yassin, F. S. Al-Mubaddel and M. T. Amen, *Appl. Catal., A*, 2018, **555**, 148–154.
35 Y. Liu, K. Li, Y. Liu, L. Pu, Z. Chen and S. Deng, *J. Mater. Chem. A*, 2015, **3**, 21149–21158.
36 G. F. Chen, T. Y. Ma, Z. Q. Liu, N. Li, Y. Z. Su, K. Davey and S. Z. Qiao, *Adv. Funct. Mater.*, 2016, **26**, 3314–3323.
37 Y. Lu, L. Wang, Z. Lou, L. Wang, Y. Zhao, W. Sun, L. Lv, Y. Wang and S. Chen, *Batteries*, 2023, **9**, 313.
38 A. Medrano-Banda, J. Guehl, G. Kéranguéven, A. Oshchepkov, E. Savinova and A. Bonnefont, *Electrochim. Acta*, 2024, **476**, 143692.
39 V. Vij, S. Sultan, A. M. Harzandi, A. Meena, J. N. Tiwari, W.-G. Lee, T. Yoon and K. S. Kim, *ACS Catal.*, 2017, **7**, 7196–7225.
40 E. Cossar, M. S. E. Houache, Z. Zhang and E. A. Baranova, *J. Electroanal. Chem.*, 2020, **870**, 114246.
41 O. González-Meza, E. Larios-Durán, A. Gutiérrez-Becerra, N. Casillas, J. Escalante and M. Bárcena-Soto, *J. Solid State Electrochem.*, 2019, **23**, 3123–3133.
42 R. Seeber, C. Zanardi and G. Inzelt, *ChemTexts*, 2016, **2**, 8.
43 Y. Zhang, J. Zhang and J. Huang, *J. Phys. Chem. Lett.*, 2019, **10**, 7037–7043.
44 A. Gupta, C. A. Allison, A. Kumar, R. Srivastava, M. Sim, J. Horinek, W. Lin, F. M. de Souza, S. R. Mishra and F. Perez, *J. Energy Storage*, 2024, **75**, 109598.
45 N. A. Barakat, I. Mustafa, G. Edris, H. Gamal and R. Osama, *Results Eng.*, 2025, 107473.
46 K. C. Pillai, G. Muthuraman and I.-S. Moon, *Electrochim. Acta*, 2017, **232**, 570–580.